J. Fluid Mech. (2024), *vol*. 987, A8, doi:10.1017/jfm.2024.387

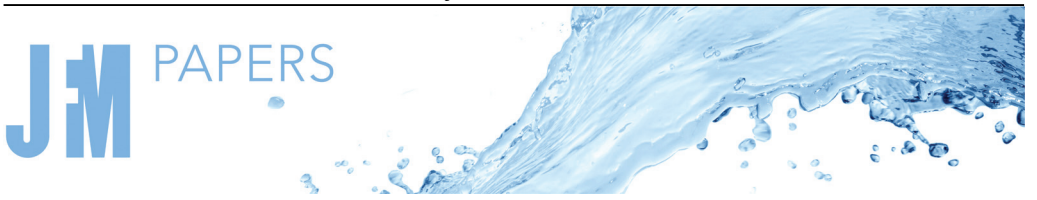

Turbulence and mixing from neighbouring stratified shear layers

Chih-Lun Liu[1],†, **Alexis K. Kaminski**[2] **and William D. Smyth**[1]

[1]College of Earth, Ocean and Atmospheric Sciences, Oregon State University, Corvallis, OR 97331, USA

[2]Department of Mechanical Engineering, University of California, Berkeley, Berkeley, CA 94720, USA

(Received 13 November 2023; revised 7 March 2024; accepted 15 April 2024)

Studies of Kelvin–Helmholtz (KH) instability have typically modelled the initial mean flow as an isolated stratified shear layer. However, geophysical flows frequently exhibit multiple layers. As a step towards understanding these flows, we examine the case of two adjacent stratified shear layers using both linear stability analysis and direct numerical simulations. With sufficiently large layer separation, the characteristics of instability and mixing converge towards the familiar KH turbulence, and similarly when the separation is near zero and the layers add to make a single layer, albeit with a reduced Richardson number. Here, our focus is on intermediate separations, which produce new and complex phenomena. As the separation distance D increases from zero to a critical value D_c, approximately half the thickness of the shear layer, the growth rate and wavenumber both decrease monotonically. The minimum Richardson number is relatively low, potentially inducing pairing, and shear-aligned convective instability (SCI) is the primary mechanism for transition. Consequently, mixing is relatively strong and efficient. When $D \sim D_c$, billow length is increased but growth is slowed. Despite the modest growth rate, mixing is strong and efficient, engendered primarily by secondary shear instability manifested on the braids, and by SCI occurring on the eyelids. Shear-aligned vortices are driven in part by buoyancy production; however, shear production and vortex stretching are equally important mechanisms. When $D > D_c$, neighbouring billow interactions suppress the growth of both KH instability and SCI. Strength and efficiency of mixing decrease abruptly as D_c is exceeded. As turbulence decays, layers of marginal instability may arise.

Key words: turbulent mixing, stratified turbulence, shear layer turbulence

† Email address for correspondence: chihlunl@gmail.com

1. Introduction

The accuracy of large-scale climate and ocean models depends on the parametrization of turbulent fluxes. Turbulent mixing events are often modelled using idealized shear instabilities in stratified flows. Shear instability has been observed in the stably stratified nocturnal atmospheric boundary layer (Newsom & Banta 2003; Smyth, Mayor & Lian 2023) as well as at higher elevations (Fritts *et al.* 2023). Shear instability has also been observed in a variety of oceanic contexts, including equatorial undercurrents (Moum, Nash & Smyth 2011), flows over sills (Van Haren *et al.* 2014; Chang *et al.* 2022), estuarine shear zones (Geyer *et al.* 2010; Holleman, Geyer & Ralston 2016; Tu *et al.* 2022), and the strongly stratified transition layer within the ocean surface boundary layer (Kaminski *et al.* 2021).

Previous theoretical research on shear instabilities has assumed a single, isolated stratified shear layer (e.g. Caulfield & Peltier 2000; Mashayek & Peltier 2013; Salehipour & Peltier 2015; Kaminski & Smyth 2019; Lewin & Caulfield 2021; Liu, Kaminski & Smyth 2022, 2023), neglecting the potential influence of nearby flow structures. Our goal here is to relax the assumption of a single, isolated shear layer. As a starting point, we examine a pair of shear layers, varying the distance between them and analysing the resulting changes in the route to turbulence and in the resulting mixing.

This is the third in a sequence of three studies using ensembles of direct numerical simulations with small, random variations in the initial state. Liu *et al.* (2022) (hereafter L22) showed that even a slight change in the initial perturbation can lead to significant variations in turbulence timing and strength due to interactions between the primary Kelvin–Helmholtz (KH), subharmonic, and three-dimensional (3-D) secondary instabilities. This resulted in differences of up to a factor of four in the maximum turbulent kinetic energy, and a factor of two in the potential energy gain due to mixing. Liu *et al.* (2023) (hereafter L23) studied the effects of boundary proximity on KH instability. Boundary effects have a pronounced effect on the dynamics of KH instability, influencing its growth, secondary instability, and the resulting turbulent mixing. Notably, the cumulative mixing efficiency vanishes as the shear layer approaches a solid boundary. As in L22, these results were sensitive to small changes in the initial conditions, emphasizing the need to compare ensemble-averaged statistics.

Our work is motivated in part by observations of multiple stratified shear layers in geophysical fluids at consecutive depths, sometimes in close proximity to each other (Desaubies & Smith 1982; Alford & Pinkel 2000). Fritts *et al.* (2003) showed layered structures in the atmosphere due to shear instability and gravity-wave breaking. Recent work on stratified shear flows reveals spontaneous organization into layers of quiescent, strongly stratified fluid and strongly turbulent, weakly stratified fluid (Woods 1968; Caulfield 2021). We therefore wonder about conditions under which instabilities of nearby shear layers could interact, and with what effect on instability, turbulence and mixing.

We find that as the separation distance between the two layers decreases to (approximately) the layer thickness, instability is suppressed. We also show that the presence of a neighbouring shear layer can excite one of two novel forms of instability, one stationary and one oscillatory. This distinction has profound effects on the transition to turbulence and the resulting mixing, including an abrupt change in mixing efficiency, even when the difference in initial states is small.

In § 2 we describe the set-up for our numerical simulations and the choice of the initial parameter values, as well as the diagnostic tools required for the analysis of 3-D energetics and mixing. We then describe the effects of neighbouring shear instability on the linear stability characteristics in § 3, and introduce the stationary and oscillatory modes of instability. In § 4, we analyse the perturbation kinetic energy budget to explain how a

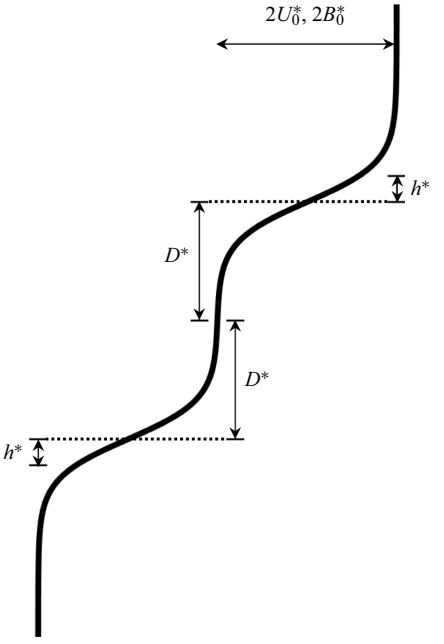

Figure 1. Initial mean profile for velocity and buoyancy showing dimensional parameters as defined in (2.1) and (2.2).

neighbouring shear instability could alter the route to turbulence. In § 5, we describe the neighbouring effects on the irreversible mixing and mixing efficiency. Conclusions are summarized in § 6, and possible directions for future research are discussed in § 7.

2. Methodology

2.1. *The mathematical model*

We begin by considering a stably stratified parallel shear flow,

$$U^*(z) = U_0^* \left[\tanh\left(\frac{z^* - D^*}{h^*} \right) + \tanh\left(\frac{z^* + D^*}{h^*} \right) \right] \tag{2.1}$$

and

$$B^*(z) = B_0^* \left[\tanh\left(\frac{z^* - D^*}{h^*} \right) + \tanh\left(\frac{z^* + D^*}{h^*} \right) \right], \tag{2.2}$$

in which $2U_0^*$ and $2B_0^*$ are, respectively, velocity and buoyancy differences across the individual shear layer, and $2h^*$ is its thickness (figure 1). Both stratified shear layers are at a distance D^* from the centre of the domain (so that the distance between the centres is $2D^*$). The domain has a vertical extent L_z^* with upper and lower boundaries at $\pm L_z^*/2$. Asterisks indicate dimensional quantities. The Cartesian coordinates are x^* (streamwise), y^* (spanwise) and z^* (vertical, positive upwards), and the corresponding velocity components are u^*, v^* and w^*. After non-dimensionalizing velocities by U_0^*, buoyancy by B_0^*, lengths by h^*, and times by the advective time scale h^*/U_0^*, (2.1) and

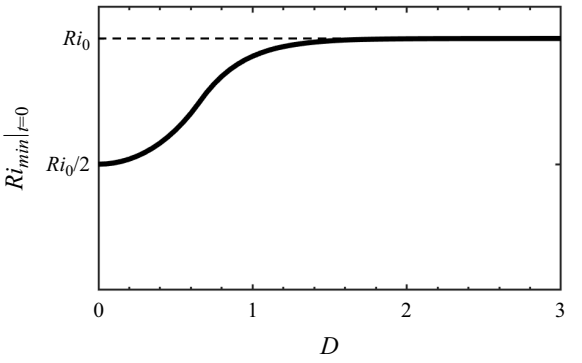

Figure 2. The dependence of initial minimum Richardson number Ri_{min} on D. Here, Ri_0 is 0.16.

(2.2) become

$$U(z) = B(z) = \tanh(z - D) + \tanh(z + D). \tag{2.3}$$

The evolution of the flow is governed by the Boussinesq Navier–Stokes equations, as well as the equations of buoyancy conservation and mass continuity. Non-dimensionalized, these are

$$\frac{\partial \boldsymbol{u}}{\partial t} + \boldsymbol{u} \cdot \nabla \boldsymbol{u} = -\nabla p + Ri_0\, b\hat{\boldsymbol{z}} + \frac{1}{Re_0} \nabla^2 \boldsymbol{u}, \tag{2.4}$$

$$\frac{\partial b}{\partial t} + \boldsymbol{u} \cdot \nabla b = \frac{1}{Re_0\, Pr} \nabla^2 b, \tag{2.5}$$

$$\nabla \cdot \boldsymbol{u} = 0, \tag{2.6}$$

where p is the pressure, and $\hat{\boldsymbol{z}}$ is the vertical unit vector. The equations involve three dimensionless parameters: the initial Reynolds number $Re_0 = U_0^* h^*/\nu^*$, where ν^* is the kinematic viscosity, the Prandtl number $Pr = \nu^*/\kappa^*$, where κ^* is the diffusivity, and the initial bulk Richardson number $Ri_0 = B_0^* h^*/U_0^{*2}$.

In general, we define the gradient Richardson number as

$$Ri_g(z, t) = \frac{\partial \langle b^* \rangle_{xy}/\partial z^*}{(\partial \langle u^* \rangle_{xy}/\partial z^*)^2} = Ri_0 \frac{\partial \langle b \rangle_{xy}/\partial z}{(\partial \langle u \rangle_{xy}/\partial z)^2} = \frac{N^2}{S^2}. \tag{2.7}$$

Here, the notation $\langle \cdot \rangle_r$ represents an average over r, where r can encompass any combination of x, y, z and t. Also, N^2 is the squared buoyancy frequency, and S is the mean shear. The minimum of Ri_g with respect to z is denoted as $Ri_{min}(t)$. In the inviscid limit, a necessary condition for instability is that Ri_{min} be less than $1/4$ (Howard 1961; Miles 1961). For the flow described by (2.3), the initial Ri_{min} increases from $Ri_0/2$ to Ri_0 when D increases from 0 to infinity (figure 2).

Boundary conditions are periodic in both horizontal directions, with periodicity intervals L_x and L_y. The upper and lower boundaries are free-slip ($\partial u/\partial z = \partial v/\partial z = 0$), insulating ($\partial b/\partial z = 0$) and impermeable ($w = 0$).

A small, random velocity perturbation is incorporated into the initial state (2.3). This initial perturbation field is purely stochastic and is applied uniformly to all three velocity components across the computational domain. The maximum amplitude of any single component is limited to 0.05, equivalent to 2.5 % of the velocity change across each

D	(L_x, L_y, L_z)	(N_x, N_y, N_z)	Ri_{min}
0	(28.56, 7.14, 30)	(576, 144, 613)	0.08
0.5	(36.96, 9.24, 30)	(768, 192, 613)	0.10
1	(78.54, 19.64, 30)	(1536, 384, 613)	0.15
2	(29.92, 7.48, 30)	(576, 144, 613)	0.16
3	(28.56, 7.14, 30)	(576, 144, 613)	0.16
∞	(27.76, 6.94, 20)	(512, 128, 361)	0.16

Table 1. Parameter values for five 3-member direct numerical simulations ensembles. In all cases, $Re_0 = 1000$, $Pr = 1$, $Ri_0 = 0.16$. Data for the case $D = \infty$ are sourced from L22 and include only a single, isolated shear layer. The maximum initial random velocity component is 0.05.

shear layer. This magnitude is kept small to ensure that the initial growth phase is consistent with linear perturbation theory. For each value of D, an ensemble of three cases is simulated, each using a distinct seed to generate the random velocities (L22).

2.2. *Linear stability analysis*

To evaluate the linear instabilities, (2.4)–(2.6) are linearized about the initial base flow (2.3). These equations are then subjected to perturbations induced by small-amplitude, normal mode disturbances proportional to the real part of $a(z)\exp(\sigma t + \mathrm{i}kx)$. In this context, $a(z)$ denotes the vertically varying, complex amplitude of any perturbation quantity, σ stands for the complex exponential growth rate, and k is the wavenumber in the streamwise direction. The streamwise phase speed is $c = \mathrm{i}\sigma/k$. The normal mode equations are discretized using a Fourier–Galerkin method, yielding a generalized matrix eigenvalue problem that is solved using standard methods. Details may be found in § 13.3 of Smyth & Carpenter (2019) or in Lian, Smyth & Liu (2020).

2.3. *Direct numerical simulations*

Simulations are conducted using DIABLO (Taylor 2008), which utilizes a hybrid implicit–explicit time-stepping scheme with pressure projection. The viscous and diffusive components are addressed implicitly using a second-order Crank–Nicolson method, while other terms are explicitly resolved employing a third-order Runge–Kutta–Wray method. The vertical z direction dependence is discretized using second-order finite differences, whereas the periodic streamwise and spanwise directions (x, y) are managed using the Fourier pseudo-spectral method.

To allow subharmonic mode growth, we set the streamwise periodicity interval L_x to two wavelengths of the fastest-growing KH mode, as determined through linear stability analysis (§ 2.2). For the development of 3-D secondary instabilities, a spanwise periodicity interval of $L_y = L_x/4$ is adequate (e.g. Klaassen & Peltier 1985; Mashayek & Peltier 2013). The domain height is $L_z = 30$ to minimize boundary effects. The computational grid is uniform and isotropic, and resolves $\sim$2.5 times the Kolmogorov length scale $L_k = (Re^{-3}/\epsilon)^{1/4}$, with ϵ representing a characteristic viscous dissipation rate after turbulence onset (e.g. Smyth & Moum 2000). Grid sizes are given in table 1.

Given the sensitivity of turbulent flows to initial conditions, we work with ensemble mean statistics where appropriate. Following L22, we use an ensemble of three cases at each separation distance D. Five values of D are considered, for a total of 15 simulations

(listed in table 1). We also employ a three-member ensemble of simulations of a single shear layer described in L22 to represent the limiting case $D \to \infty$.

To maintain our primary focus on the influence of the adjacent shear layer, we keep the initial state parameters, specifically the Richardson, Reynolds and Prandtl numbers, fixed. The choice $Ri_0 = 0.16$ is large enough for the pairing instability (e.g. Klaassen & Peltier 1989) to be damped by stratification when $Ri_{min} = Ri_0$ (i.e. for large D). In all cases, we set $Re_0 = 1000$ and $Pr = 1$. While smaller than would be typical in nature, these values reflect a necessary compromise dictated by computational resource constraints.

2.4. *Diagnostics*

The total velocity field can be decomposed into a horizontally averaged component, referred to as the mean flow, and a perturbation

$$\boldsymbol{u}(x, y, z, t) = \bar{U}\,\hat{\boldsymbol{e}}^{(x)} + \boldsymbol{u}'(x, y, z, t), \quad \text{where } \bar{U}(z, t) = \langle u \rangle_{xy}\,, \tag{2.8}$$

with $\hat{\boldsymbol{e}}^{(x)}$ the unit vector in the streamwise direction. Following Caulfield & Peltier (2000), the perturbation velocity is further subdivided into two-dimensional (2-D) and 3-D components:

$$\boldsymbol{u}'(x, y, z, t) = \boldsymbol{u}_{2d} + \boldsymbol{u}_{3d}, \tag{2.9}$$

where

$$\boldsymbol{u}_{2d}(x, z, t) = \langle \boldsymbol{u} \rangle_y - \bar{U}\,\hat{\boldsymbol{e}}^{(x)} \quad \text{and} \quad \boldsymbol{u}_{3d}(x, y, z, t) = \boldsymbol{u} - \boldsymbol{u}_{2d} - \bar{U}\,\hat{\boldsymbol{e}}^{(x)} = \boldsymbol{u} - \langle \boldsymbol{u} \rangle_y\,. \tag{2.10a,b}$$

Similarly, the buoyancy field can be decomposed as

$$b(x, y, z, t) = \bar{B} + b'(x, y, z, t), \quad \text{where } \bar{B}(z, t) = \langle b \rangle_{xy}, \tag{2.11}$$

$$b_{3d}(x, y, z, t) = b - \langle b \rangle_y. \tag{2.12}$$

The total kinetic energy can now be partitioned as

$$\mathscr{K} = \bar{\mathscr{K}} + \mathscr{K}', \quad \mathscr{K}' = \mathscr{K}_{2d} + \mathscr{K}_{3d}, \tag{2.13a,b}$$

where

$$\bar{\mathscr{K}} = \tfrac{1}{2}\langle \bar{U}^2 \rangle_z, \quad \mathscr{K}_{2d} = \tfrac{1}{2}\langle u_{2d}^2 + v_{2d}^2 + w_{2d}^2 \rangle_{xz}, \quad \mathscr{K}_{3d} = \tfrac{1}{2}\langle u_{3d}^2 + v_{3d}^2 + w_{3d}^2 \rangle_{xyz}. \tag{2.14a–c}$$

These constituent kinetic energies $\bar{\mathscr{K}}$, $\mathscr{K}'$, $\mathscr{K}_{2d}$ and $\mathscr{K}_{3d}$ can be identified as the horizontally averaged kinetic energy associated with the mean flow, the turbulent kinetic energy, and the kinetic energy related to 2-D and 3-D motions. We denote the instances in time when $\mathscr{K}_{2d}$ and $\mathscr{K}_{3d}$ reach their maximum values as t_{2d} and t_{3d}, respectively.

Quantification of irreversible mixing involves decomposing the total potential energy $\mathscr{P} = -Ri_0\,\langle bz \rangle_{xyz}$ into available and background components, $\mathscr{P} = \mathscr{P}_a + \mathscr{P}_b$. The background potential energy $\mathscr{P}_b$ is the minimum potential energy achievable by adiabatically rearranging the buoyancy field into a statically stable state b^* (Winters *et al.* 1995; Tseng & Ferziger 2001). After computing the total and background potential energies, the available potential energy is determined from the residual, $\mathscr{P}_a = \mathscr{P} - \mathscr{P}_b$. Here, $\mathscr{P}_a$ represents the potential energy available for conversion to kinetic energy, arising from lateral variations in buoyancy or statically unstable regions.

The irreversible mixing rate due to fluid motions is defined as

$$\mathscr{M} = \frac{\mathrm{d}\mathscr{P}_b}{\mathrm{d}t} - \mathscr{D}_p, \tag{2.15}$$

where

$$\mathscr{D}_p = \frac{Ri_0\,(b_{top} - b_{bottom})}{Re_0\,Pr\,L_z} \tag{2.16}$$

refers to the rate at which the potential energy of a statically stable buoyancy distribution would increase solely due to diffusion of the mean buoyancy profile in the absence of any fluid motion.

There exists a variety of definitions for mixing efficiency in the literature (e.g. Gregg *et al.* 2018). Here, we define the instantaneous mixing efficiency as

$$\eta_i = \frac{\mathscr{M}}{\mathscr{M} + \epsilon}, \tag{2.17}$$

where $\epsilon = (2/Re)\langle s_{ij}s_{ij}\rangle_{xyz}$ is the total dissipation rate, and $s_{ij} = (\partial u_i/\partial x_j + \partial u_j/\partial x_i)/2$ is the strain rate tensor. The mixing efficiency quantifies the fraction of energy directed towards irreversible mixing to the total kinetic energy loss that is irreversibly lost to friction (Peltier & Caulfield 2003). The cumulative mixing efficiency serves as a valuable measure for quantifying the overall efficiency of the entire mixing process, and is defined as

$$\eta_c = \frac{\displaystyle\int_{t_i}^{t_f} \mathscr{M}\,\mathrm{d}t}{\displaystyle\int_{t_i}^{t_f} \mathscr{M}\,\mathrm{d}t + \int_{t_i}^{t_f} \epsilon\,\mathrm{d}t}, \tag{2.18}$$

where $t_i \sim 2$ is the initial time after the model adjustment period, and t_f is the final time of the integral at which $\mathscr{M} = \mathscr{D}_p$.

An alternative quantifier of mixing that readily shows the spatial structure is the perturbation buoyancy variance dissipation rate, defined as

$$\chi'(x, y, z, t) = \frac{2\,Ri_0}{Re\,Pr}\,|\nabla b'|^2, \tag{2.19}$$

where b' is the buoyancy perturbation, representing the deviation from the horizontal mean buoyancy.

The evolution equation for the kinetic energy of 3-D perturbations can be expressed in the form (Caulfield & Peltier 2000)

$$\sigma_{3d} = \frac{1}{2\mathscr{K}_{3d}}\frac{\mathrm{d}}{\mathrm{d}t}\mathscr{K}_{3d} \tag{2.20}$$

$$= \mathscr{R}_{3d} + \mathscr{SH}_{3d} + \mathscr{A}_{3d} + \mathscr{H}_{3d} + \mathscr{D}_{3d}, \tag{2.21}$$

where the first two terms represent the 3-D perturbation kinetic energy extraction from the background mean shear and the background 2-D KH billow by means of Reynolds

stresses, respectively defined as

$$\mathscr{R}_{3d} = -\frac{1}{2\mathscr{K}_{3d}}\left\langle u_{3d}w_{3d}\frac{\partial \bar{U}}{\partial z}\right\rangle_{xyz}, \tag{2.22}$$

$$\mathscr{SH}_{3d} = -\frac{1}{2\mathscr{K}_{3d}}\left\langle u_{3d}w_{3d}\left(\frac{\partial u_{2d}}{\partial z}+\frac{\partial w_{2d}}{\partial x}\right)\right\rangle_{xyz}. \tag{2.23}$$

The third term represents the stretching deformation of the 3-D motions and is defined as

$$\mathscr{A}_{3d} = -\frac{1}{2\mathscr{K}_{3d}}\left\langle \frac{1}{2}\left(u_{3d}^2 - w_{3d}^2\right)\left(\frac{\partial u_{2d}}{\partial x}-\frac{\partial w_{2d}}{\partial z}\right)\right\rangle_{xyz}. \tag{2.24}$$

The final two terms are the buoyancy production term and the negative-definite viscous dissipation term associated with 3-D perturbations, and are defined respectively as

$$\mathscr{H}_{3d} = \frac{Ri_0}{2\mathscr{K}_{3d}}\langle b_{3d}w_{3d}\rangle_{xyz}, \tag{2.25}$$

$$\mathscr{D}_{3d} = -\frac{1}{\mathscr{K}_{3d}\,Re}\langle s_{ij}s_{ij}\rangle_{xyz}, \tag{2.26}$$

where s_{ij} is the strain rate tensor of the 3-D motions. The time at which σ_{3d} is a maximum is defined as $t_{\sigma_{3d}}$. The enstrophy in the three vorticity components is defined as

$$\mathscr{Z}_x = \tfrac{1}{2}(\omega_x^2), \quad \mathscr{Z}_y = \tfrac{1}{2}(\omega_y^2), \quad \mathscr{Z}_z = \tfrac{1}{2}(\omega_z^2), \tag{2.27a–c}$$

where

$$\omega_x = \frac{\partial w}{\partial y}-\frac{\partial v}{\partial z}, \quad \omega_y = \frac{\partial u}{\partial z}-\frac{\partial w}{\partial x} \quad \text{and} \quad \omega_z = \frac{\partial v}{\partial x}-\frac{\partial u}{\partial y}. \tag{2.28a–c}$$

3. The primary linear instability

In the extreme cases, $D = 0$ and $D \to \infty$, (2.3) is equivalent to one or two isolated shear layers that produce standard KH instabilities (e.g. Hazel 1972; Smyth & Carpenter 2019) if $Ri_0 < 1/4$. In the previously unexplored cases with finite, non-zero D, (2.3) represents a superposition of two shear layers whose modes of instability interact in complex ways.

In the case $D = 0$, (2.3) becomes $U(z) = B(z) = 2\tanh(z)$, i.e. the two shear layers sum to make a single stratified shear layer with doubled shear and stratification (dark blue curve in figure 3). The corresponding Ri_{min} is $Ri_0/2 = 0.08$. The dominant mode is the stationary KH mode, with a fastest-growing wavenumber 0.44. We term this a stationary mode because there is only a single fastest-growing mode for a given initial state. (This is in contrast to oscillatory instability, discussed below, which is a superposition of two modes with equal growth rates but different phase speeds.) In the reference frame assumed here, the phase speed of the stationary mode is zero, while the two phase speeds of the oscillatory mode are opposites.

As D increases to $\tanh^{-1}\sqrt{1/3}$ (approximately 0.66), the single shear maximum at $z = 0$ widens (light blue curve in figure 3*b*). Therefore, the wavenumber of the fastest-growing mode decreases, the growth rate decreases (figure 4, red curve), and Ri_{min} increases (figure 3(*c*), light blue curve). The corresponding mode is a continuation of the stationary mode found at $D = 0$ as discussed above. It may be thought of as a KH-like instability of the two shear layers *in toto*, rather than of one or the other layer.

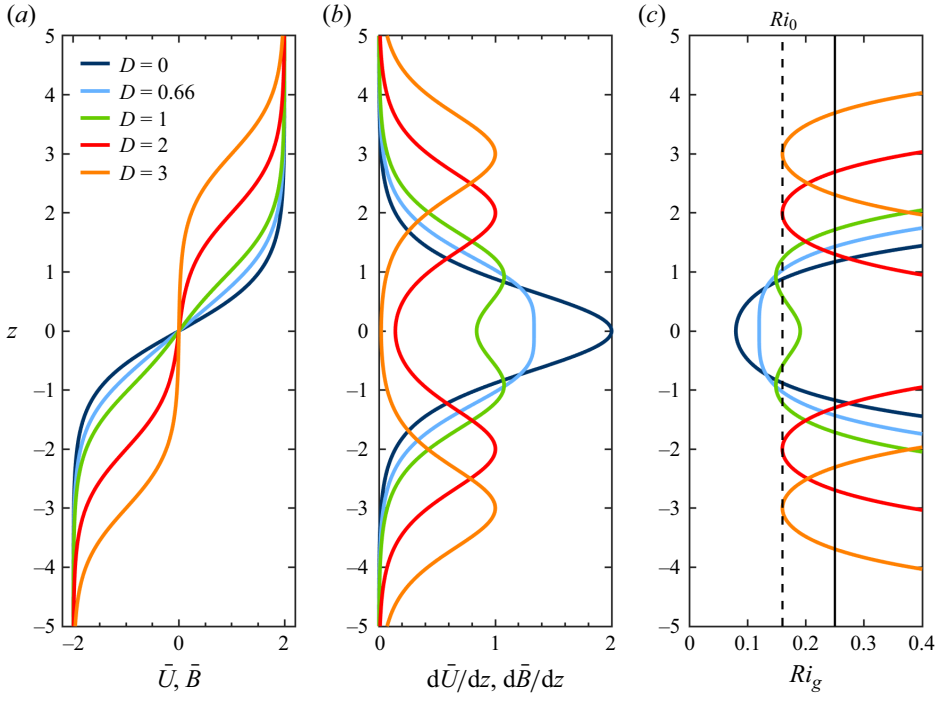

Figure 3. Profiles of (*a*) horizontally averaged velocity and buoyancy, (*b*) mean velocity and mean buoyancy gradient, and (*c*) gradient Richardson number. The vertical dashed line in (*c*) shows Ri_0, and the vertical solid line denotes the stability criterion 1/4.

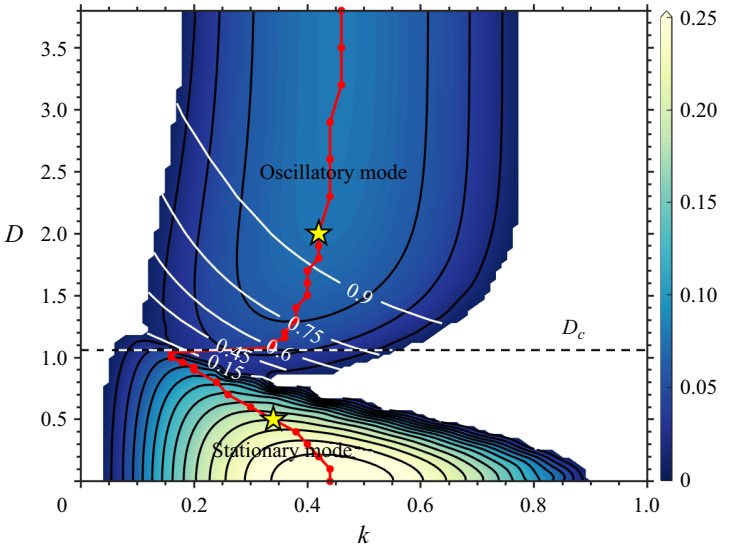

Figure 4. Stability diagram showing the transition from the stationary mode to the oscillatory mode as D increases, with $Re = 1000$, $Pr = 1$, $Ri_0 = 0.16$, and boundaries at $z = \pm L_z/2 = \pm 15$. Colours and black contours represent the growth rate of the fastest-growing mode on the k–D plane. The contour interval is 0.02. White contours show the (positive) phase velocity. The horizontal dashed line denotes the critical distance D_c ($= 1.06$). Stars highlight the cases $D = 0.5$ and $D = 2$, where the eigenfunctions of the fastest-growing modes are shown in figure 7.

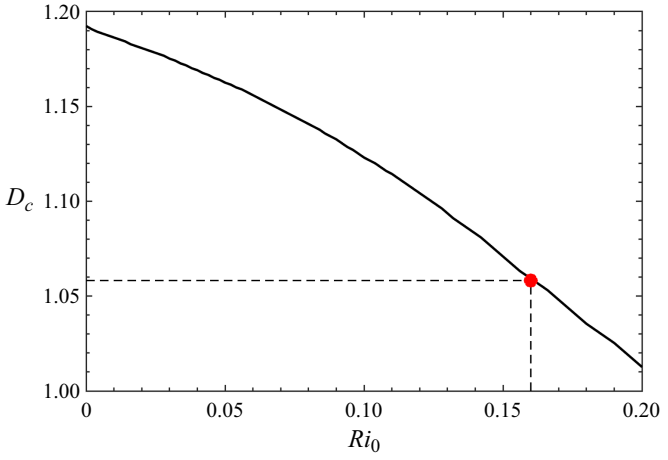

Figure 5. The dependence of critical distance D_c on Ri_0. The corresponding D_c for $Ri_0 = 0.16$ is $\sim$1.06, as shown by the red dot.

If D slightly exceeds $\tanh^{-1}\sqrt{1/3}$, then two small shear maxima appear slightly above and below $z = 0$. These produce two inflectional instabilities having equal (though small) growth rates, and equal but opposite phase velocities. (Only the positive phase velocity is shown in figure 4.) Combined, these modes result in an oscillatory instability. As D increases further, the oscillatory and stationary modes coexist (figure 4). The shear maxima become weaker but more distinct (green curve in figure 3*b*). The growth rate of the oscillatory mode increases, while that of the stationary mode continues to decrease (figure 4). The two modes attain equal growth rates at a critical separation distance $D = D_c$, with $D_c = 1.06$ in the present case, $Ri_{min} = 0.16$ (dashed horizontal lines in figures 4 and 5). More generally, D_c decreases slightly with increasing Ri_0 (figure 5).

At higher D (approximately 1.2 in our case), the stationary mode is stabilized, while the growth rate of the oscillatory mode continues to increase with increasing D (figure 4). When $D = 3$, for example, the two shear maxima are separated by a weakly stratified layer (orange curve in figure 3). The resulting pair of modes have equal growth rates and opposite phase velocities. They combine to form the oscillatory mode. As $D \to \infty$, the upper and lower instabilities that form the oscillatory mode are independent, stationary KH modes with unequal phase speeds.

We next explore the effects of varying Ri_0 (figure 6). When $D = 0$, the stability boundary for the two superimposed shear layers can be written as $Ri_0 = 2k(1-k)$, neglecting viscosity and assuming an infinite domain (e.g. Smyth & Carpenter 2019). This results in the instability criterion $Ri_0 < 1/2$. Figure 6(*a*) depicts the growth rate in the k–Ri_0 plane. (Positive values lying outside the theoretical stability boundary are an artefact of the finite vertical domain size; cf. Hazel 1972.) The stationary mode dominates for $D = 0$ and 0.5 (figures 6*a*,*b*). As D increases from 0 to 0.5, the unstable modes shift towards lower wavenumbers. When $D = 1$, the stationary mode is the fastest-growing mode, and its associated fastest-growing wavenumber decreases to less than 0.2 for all Ri_0 (figure 6*c*). At higher wavenumbers, the oscillatory mode dominates. With an increase in D to 3, the upper and lower shear layers become widely separated, resulting in the disappearance of the stationary mode and the dominance of the oscillatory mode (see figure 6*d*). The stability boundary under the inviscid limit, depicted as the dashed curve, aligns well with the numerical results. This alignment suggests that, at least within the

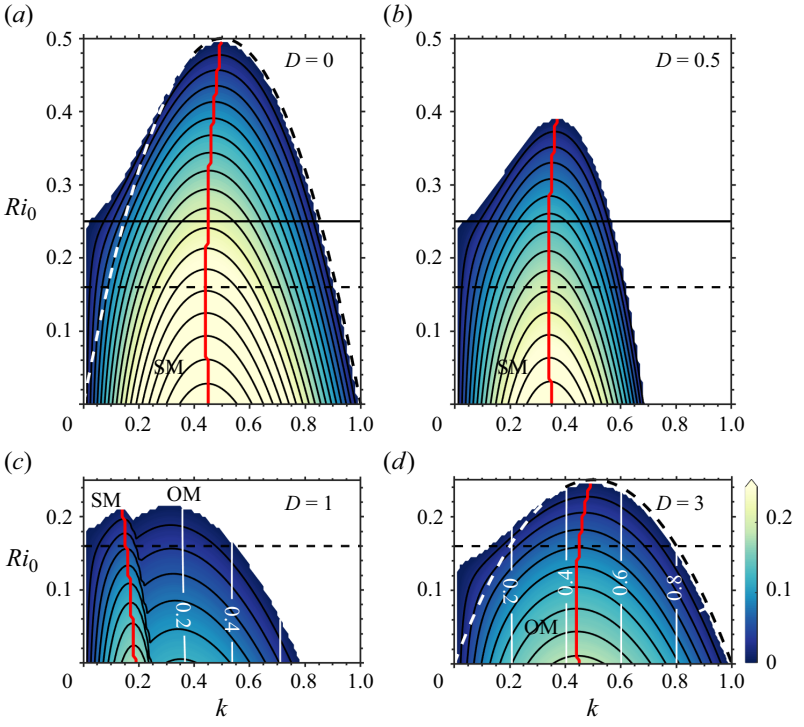

Figure 6. Stability diagram illustrating the transition from the stationary mode (SM) to the oscillatory mode (OM) as D increases, with $Re = 1000$, $Pr = 1$, and boundaries at $z = \pm L_z/2 = \pm 15$. Colours and black contours represent the growth rate on the k–D plane for different values of D: (*a*) $D = 0$, (*b*) $D = 0.5$, (*c*) $D = 1$, and (*d*) $D = 3$. The fastest growth rate at each k, Ri_0 is shown. The contour interval is 0.02. White contours represent the corresponding frequency σ_i. The red curve denotes the fastest-growing mode at each Ri_0. Dashed curves show the inviscid stability boundary for an infinite domain, $Ri_0 = 2k(1-k)$ when $D = 0$ in (*a*), and $Ri_0 = k(1-k)$ for the single tanh profile considered in (*d*). The horizontal dashed line and solid line show $Ri_0 = 0.16$ and $Ri_0 = 0.25$, respectively.

linear regime, the configuration with $D = 3$ resembles a pair of isolated shear layers. To summarize, figure 6 shows that the modal structure in the linear regime is remarkably insensitive to the choice of Ri_0; at each D, we see only the expected decrease of growth rate with increasing Ri_0. In what follows, we will focus on the case $Ri_0 = 0.16$.

We next examine the vertical structures of typical stationary and oscillatory modes. The eigenfunction of the stationary mode at $D = 0.5$ (figure 7*a*) displays symmetry about $z = 0$, characteristic of KH instability (e.g. Smyth & Peltier 1989). The corresponding phase speed is zero (figure 7*a*). When $D = 2$, modes are associated with the upper and lower shear layers. The corresponding eigenfunctions are reflections of each other about $z = 0$ (figures 7*b*,*c*). While upper and lower modes share identical growth rates σ_r, their phase speeds are equal but opposite, so that their sum has an oscillatory, standing-wave-like character.

To close this section, we discuss the mechanisms that cause growth rates to decrease as D approaches D_c. As $D \to D_c$ from above, the oscillatory mode is damped. To explain, we invoke the wave resonance mechanism for piecewise linear shear layers (Heifetz *et al.* 2004; Carpenter *et al.* 2013; Heifetz & Guha 2019; Smyth & Carpenter 2019). The schematic representation in figure 8(*a*) shows a piecewise linear velocity profile with four kinks (i.e. vorticity discontinuities). Correspondingly, figure 8(*b*) depicts the

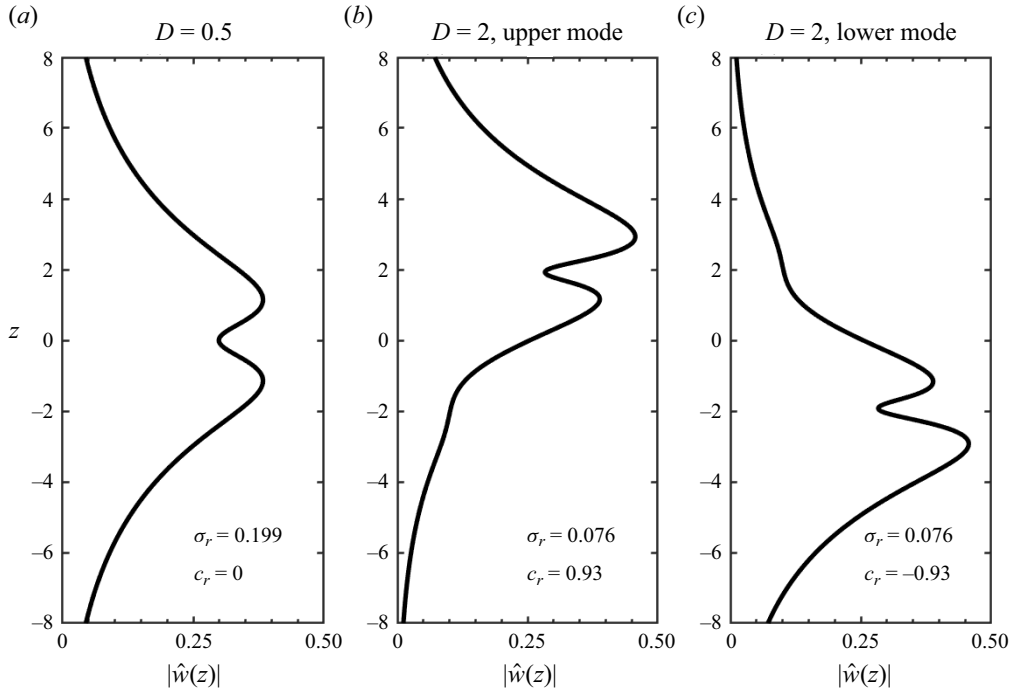

Figure 7. (*a*) Magnitudes of the vertical velocity eigenfunction $\hat{w}$ for the fastest-growing mode when $D = 0.5$. This mode corresponds to a stationary KH-like instability. (*b*,*c*) Magnitudes of the vertical velocity eigenfunction for the upper and lower modes when $D = 2$. Both of these modes are oscillatory, exhibiting identical growth rates σ_r and phase speeds c_r of equal magnitude but opposite signs.

vorticity wave associated with each kink, showing phase-locking between wave 1 and wave 2, as well as between wave 3 and wave 4, each in the phase configuration that is optimal for resonant amplification. This results in the growth of two trains of KH billows, corresponding to the oscillatory instability discussed above. When D is finite, an added interaction occurs between wave 2 and wave 3. (Interactions between waves 1 and 3, 2 and 4, and 1 and 4 are present but weaker when $D > D_c$.) The phase relationship between these waves now varies in time, owing to their opposing horizontal propagation. Figure 8(*b*) provides an example. In this particular configuration, waves 2 and 3 force each other in their own directions. The opposite can be true for other phase relationships that occur as the waves pass each other. Regardless of the horizontal propagation, waves 2 and 3 consistently perturb each other's phases, so that they cannot remain phase-locked in the optimal configuration for resonance, and the growth rate is thus reduced. This destructive interference increases as D decreases until $D = \tanh^{-1}\sqrt{1/3}$, at which point the oscillatory mode vanishes, leaving only the stationary mode.

The damping that we find as $D \to D_c$ from below (figure 4) is unsurprising because the shear maximum at $z = 0$ weakens (figure 3(*b*), compare dark blue and light blue curves), but it can also be understood in terms of wave resonance. The resonance between wave 1 and wave 2, as well as between wave 3 and wave 4, diminishes due to the disturbances between waves 2 and 3 described above. However, resonance between wave 1 and wave 4 remains strong, leading to the development of a KH-like instability. As $D \to D_c^-$, the separation between wave 1 and wave 4 increases, rendering resonance less effective.

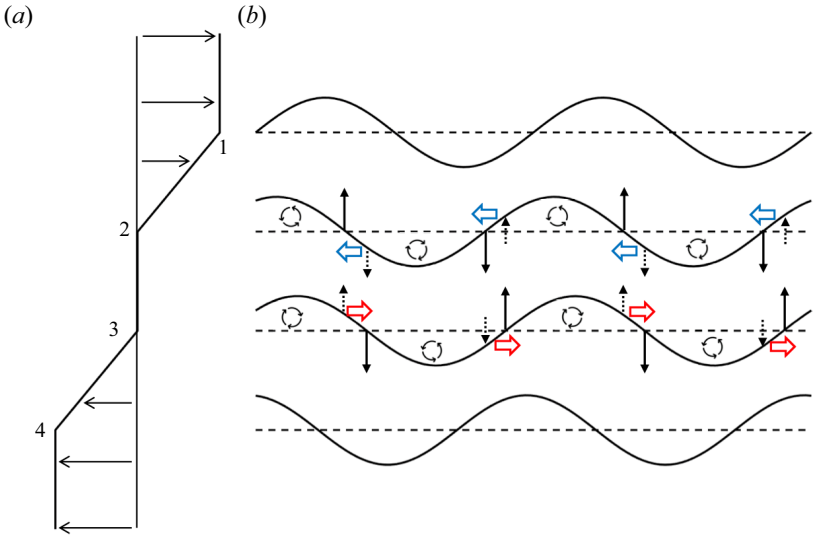

Figure 8. (*a*) Piecewise linear background velocity profile. (*b*) Vorticity wave field diagram. Waves 1 and 2 resonate to create the upper KH-like instability. The phase difference 0.35π is optimal for growth. The same is true for waves 3 and 4, which create the lower KH-like instability. The main interaction between these two instabilities involves waves 2 and 3. Counter-rotating vorticity perturbation causes alternately upward and downward motion (black solid arrows). These motions induce vertical motions to the nearby waves (black dashed arrows). Therefore, the interaction accelerates the upper wave to the left (blue arrows) and the lower wave to the right (red arrows).

4. The route to turbulence

4.1. *Overview of the nonlinear development*

In this subsection, we look beyond the linear regime to examine the various secondary instabilities that emerge at different separation distances D and trigger the transition to turbulence (see examples in figure 9). In all cases, the initial condition consists of an unstable parallel shear flow whose primary instability grows to form 2-D periodic laminar vortices. These vortices attain maximum kinetic energy at $t = t_{2d}$ (figures 9*a*,*e*,*i*). As expected, the wavelength is largest (among these three examples) for $D = 1$, and smallest for $D = 2$, where two trains of billows combine to form the oscillatory instability (figure 9*i*). In the oscillatory case, $D = 2$, the growth rate and the time of turbulence onset are sensitive to the details of the initial perturbations, as is evident in the contrast between the upper and lower billow trains (figures 9*i*,*j*). The evolution progresses at a comparatively slower rate for $D = 1$, consistent with its relatively small linear growth rate, while growth is faster for $D = 0.5$ (compare the values of t_{2d} between cases). During this progression, various secondary instabilities emerge, facilitating the breakdown of the primary KH billows (e.g. figures 9*b*,*f*,*j*). This breakdown leads to the generation of turbulence (e.g. at $t = t_{3d}$, figures 9*c*,*g*,*k*). Following the turbulent mixing phase, the flow relaminarizes (figures 9*d*,*h*,*l*).

Secondary instabilities that govern the evolution of isolated KH billows at different values of Ri_{min} have been explored in previous research (e.g. Davis & Peltier 1979; Klaassen & Peltier 1985, 1991; Mashayek & Peltier 2012*a*,*b*, 2013, L22). In §§ 4.2 and 4.3, we focus on secondary instabilities that contribute to 3-D perturbation kinetic energy in the regimes $D > D_c$ and $D < D_c$, wherein the linear development is dominated by the oscillatory and stationary modes, respectively. Pertinent examples include the central

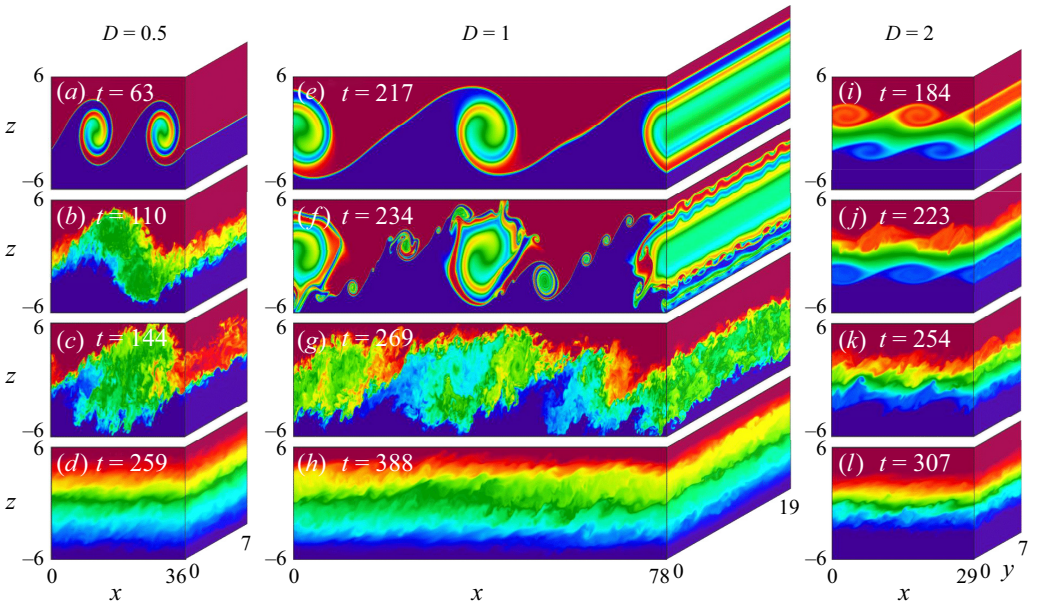

Figure 9. Cross-sections through the 3-D buoyancy field for example cases with (*a–d*) $D = 0.5$, (*e–h*) $D = 1$, and (*i–l*) $D = 2$, at successive times as indicated. The buoyancy values plotted range from -1.5 (blue) to 1.5 (red). Snapshots in (*a*,*e*,*i*) correspond to $t = t_{2d}$, in (*c*,*g*,*k*) to $t = t_{3d}$, and in (*d*,*h*,*l*) to $t = t_f$, the time when $\mathscr{M} = \mathscr{D}_p$.

core instability (CCI, e.g. Klaassen & Peltier 1991, L23), which is catalysed by the initial growth of the KH instability, and the shear-aligned convective instability (SCI, e.g. Davis & Peltier 1979; Klaassen & Peltier 1985), which manifests when KH billows reach a sufficient size to overturn the buoyancy structure. In § 4.4, we discuss 2-D secondary instabilities: the secondary shear instability (SSI) of the braids and pairing of adjacent billows (visible in figures 9(*f*) and 9(*b*), respectively).

4.2. *Regime $D > D_c$*

We examine the regime $D > D_c$, using ensembles of simulations with $D \to \infty$, $D = 3$ and $D = 2$ as examples. When the shear layers are infinitely separated ($D \to \infty$), they are independent of each other, and each exhibits the standard KH instability (e.g. L22). The 3-D perturbation kinetic energy $\mathscr{K}_{3d}$ (figure 10*a*) is created mostly by shear production $\mathscr{R}_{3d}$, which draws energy from the mean flow (blue curve). The growth of $\mathscr{R}_{3d}$ can be attributed to the sinusoidal distortion of the spanwise vortex tube at the core of each nascent KH billow, which redirects spanwise (y) vorticity towards the x–z plane. The tilt of the sinusoidal distortion is such that the Reynolds stress $\langle u_{3d} w_{3d} \rangle_{xyz}$ becomes negative (see figure 14 of Lasheras & Choi (1988), figure 9 of Smyth & Winters (2003), or figure 8 of Smyth 2006). This negative 3-D stress field works with the positive mean shear $\mathrm{d}\bar{U}/\mathrm{d}z$ to generate 3-D kinetic energy. By $t = t_{\sigma_{3d}}$ (the time of maximum 3-D growth), $\mathrm{d}\bar{U}/\mathrm{d}z$ is no longer a maximum in the billow core, but the Reynolds stress is. Therefore, the dominant contributor to energy growth, quantified by $\mathscr{R}_{3d}$, arises in this region. We identify this mode as the CCI.

The buoyancy production $\mathscr{H}_{3d}$ (red curve) is positive but much smaller than $\mathscr{R}_{3d}$. In the current case with $Ri_0 = 0.16$, previous work suggests that the SCI (signalled by positive

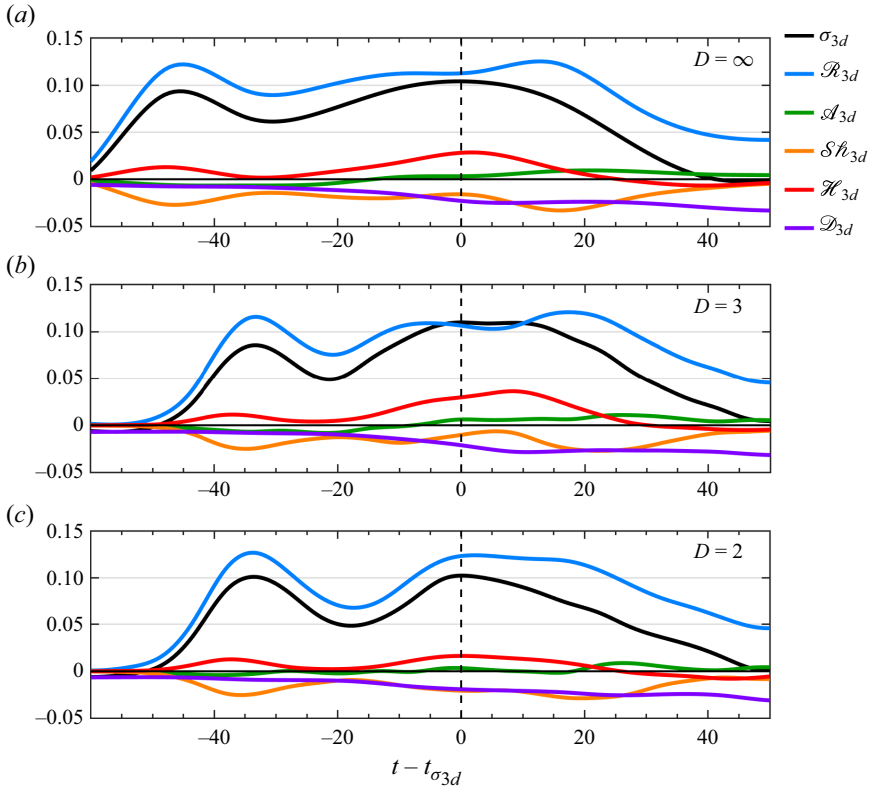

Figure 10. Time variation of terms of the σ_{3d} equation (2.21) when (*a*) $D = \infty$, (*b*) $D = 3$, and (*c*) $D = 2$. All curves are ensemble averaged. Vertical dashed lines show the time at which the growth σ_{3d} is a maximum. Note that the time for each ensemble case is shifted, such that the 3-D growth rate σ_{3d} is a maximum at $t - t_{\sigma_{3d}} = 0$. Terms except for σ_{3d} are obtained from cubic spline fits.

$\mathscr{H}_{3d}$) should be suppressed. Based on secondary stability analysis, the SCI grows only when $0.065 < Ri_0 < 0.13$ (Klaassen & Peltier 1991). The dominance of shear production $\mathscr{R}_{3d}$ and suppression of buoyancy production $\mathscr{H}_{3d}$ when $D \to \infty$ are also consistent with the findings of Mashayek, Caulfield & Peltier (2013), particularly in their case $Ri_0 = 0.16$, $Re = 6000$.

As the separation distance between two shear layers is decreased from infinity to values approaching D_c (e.g. our examples $D = 3$ and 2), interactions become evident. When $D = 3$, the evolution of each perturbation energy term resembles the infinite separation case (compare figures 10*a*,*b*), suggesting only a weak interaction between the upper and lower instabilities. When $D = 2$, $\mathscr{R}_{3d}$ remains the dominant term (i.e. the principal secondary instability is still the CCI); however, a reduction in $\mathscr{H}_{3d}$ (figure 10*c*) is observed. At $t = t_{\sigma_{3d}}$, for example, the reduction is ∼40 % compared to case $D \to \infty$. This reduction can be attributed to the close proximity of the shear layers, which results in additional suppression of SCI beyond the inherent effects of high Ri_{min}. Because the upper and lower billows co-rotate, roll-up is suppressed, reducing overturning. This is reminiscent of the effect of a nearby boundary on the SCI (L23).

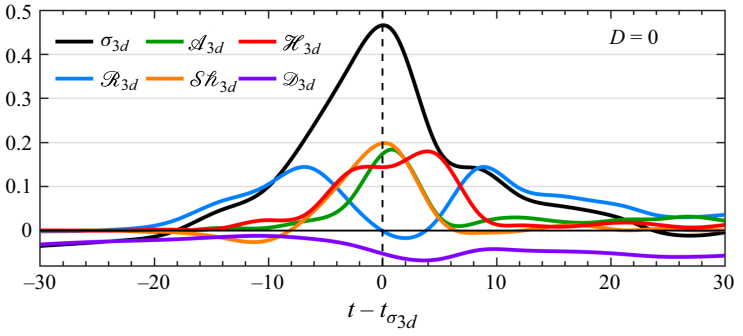

Figure 11. As in figure 10, but with $D = 0$.

4.3. *Regime $D < D_c$*

We now examine distinctions that arise when $D < D_c$, using examples $D = 0$, 0.5 and 1. When $D = 0$, the two shear layers add to form a single shear layer with $Ri_{min} = Ri_0/2 = 0.08$. Thus the instability behaves similarly to a weakly stratified shear instability, and we expect to encounter the SCI. During the earliest stage of 3-D growth ($t - t_{\sigma_{3d}} \sim -18$ to -6), the $\mathscr{K}_{3d}$ budget is dominated by the shear production term $\mathscr{R}_{3d}$ due to the CCI. By $t \sim t_{\sigma_{3d}}$, the billow has rolled up enough to form convectively unstable layers. Consistent with the low initial Ri_{min}, the SCI is now the principal secondary instability that breaks down the KH billow structure. This is indicated in the $\mathscr{K}_{3d}$ budget (figure 11) by increased values of $\mathscr{H}_{3d}$ as well as $\mathscr{S}\mathscr{h}_{3d}$ and $\mathscr{A}_{3d}$. One would expect the buoyancy production term $\mathscr{H}_{3d}$ to be substantial due to the prevailing influence of the SCI (Caulfield & Peltier 2000, L23). Surprisingly, both $\mathscr{S}\mathscr{h}_{3d}$ and $\mathscr{A}_{3d}$ exhibit larger magnitudes than $\mathscr{H}_{3d}$ (figure 11*a*). This finding is distinguished from previous studies (Mashayek & Peltier 2013, L23), where buoyancy production dominated in the presence of the SCI. This may reflect a difference in the initial perturbations; the buoyancy field was perturbed in the previous studies but not in the present work.

When D is slightly above 0 (typified here by $D = 0.5$), Ri_{min} is small enough that the KH billow is again susceptible to SCI (Klaassen & Peltier 1991). During the initial growth phase (dot-dashed line in figure 12*a*), large positive values of $\mathscr{R}_{3d}$ concentrate in the billow core, indicating the CCI. This mechanism can be discerned qualitatively in the spanwise-averaged x–z representation of $\mathscr{R}_{3d}$ (figure 12(*b*), region 1). Simultaneously, small areas of positive $\mathscr{S}\mathscr{h}_{3d}$ manifest at the upper and lower extents of the billows (figure 12(*c*), region 2). Moreover, positive $\mathscr{A}_{3d}$ emerges along the braids (figure 12(*d*), region 3). These results are associated with the mechanism illustrated in figure 12 of Lasheras & Choi (1988), which shows that vortex filaments present in the braids undergo amplification through stretching along the principal plane of positive strain. These vortex filaments eventually envelop the spanwise vortex tubes of the central core, resulting in positive $\mathscr{S}\mathscr{h}_{3d}$ in the upper and lower regions of each billow, and positive $\mathscr{A}_{3d}$ at the braids. Owing to the wrapping of these vortex filaments, the spanwise vortex tubes undulate (figure 14 in Lasheras & Choi 1988), creating positive $\mathscr{R}_{3d}$ in the core. Nonetheless, $\mathscr{S}\mathscr{h}_{3d}$ is mostly negative in the braids and in the billow cores, leading to an overall negative volume average (dashed line in figure 12*a*). Positive $\mathscr{H}_{3d}$ in the eyelids (region 4 of figure 12*e*) indicates the SCI.

At $t = t_{\sigma_{3d}}$, similar to $D = 0$, $\mathscr{H}_{3d}$ is smaller than both $\mathscr{S}\mathscr{h}_{3d}$ and $\mathscr{A}_{3d}$ (figure 12*a*). The SCI induces the formation of shear-aligned convective rolls, consistent with increased

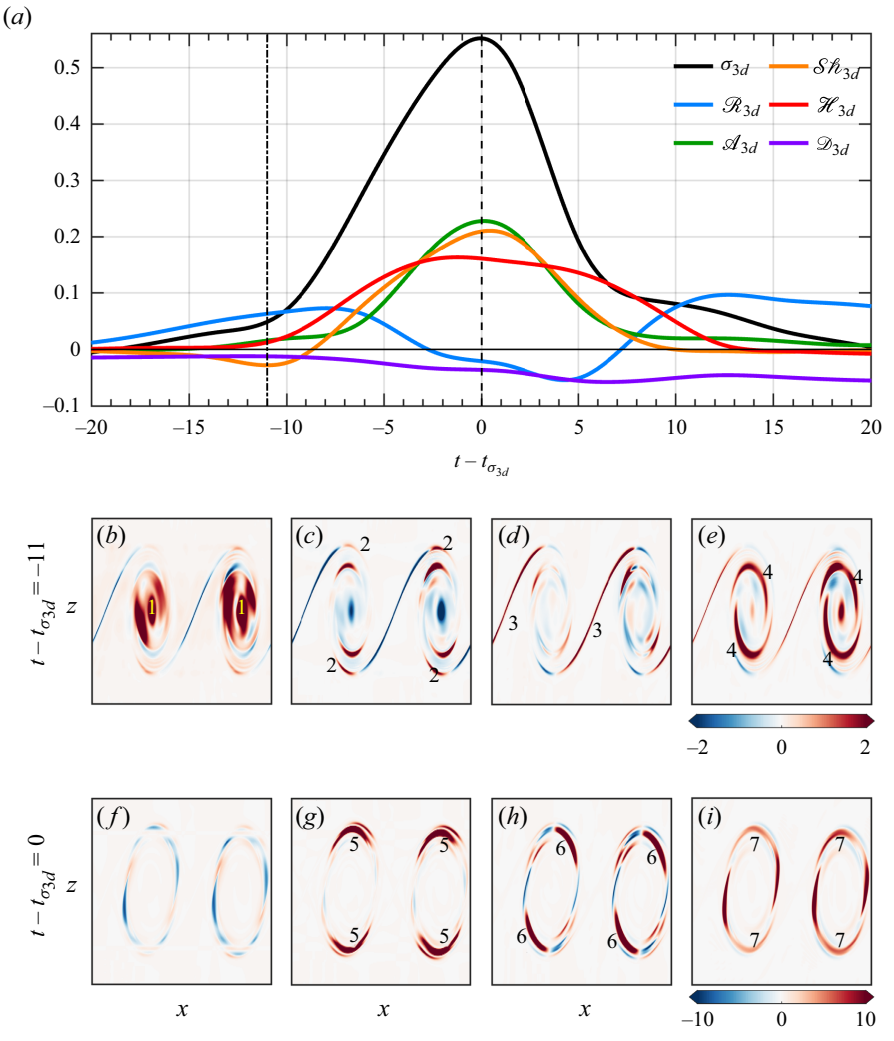

Figure 12. Dominant stationary mode when $D = 0.5$. (*a*) As in figure 10. Vertical dot-dashed line and dashed line show the times at $t - t_{\sigma_{3d}} = -11$ and 0, respectively. (*b–e*) Spatial distribution of each energy term: $\mathcal{R}_{3d}$, $\mathcal{SH}_{3d}$, $\mathcal{A}_{3d}$ and $\mathcal{H}_{3d}$, respectively, at $t_{\sigma_{3d}} = -11$ (dot-dashed line in *a*). (*f–i*) Same at $t - t_{\sigma_{3d}} = 0$ (dashed line in *a*).

buoyancy production $\mathcal{H}_{3d}$ (figure 12(*i*), region 7). Positive $\mathcal{SH}_{3d}$ coincides with these convective rolls (region 5), suggesting that the SCI could be responsible for its generation. During the early growth phase, $\mathcal{H}_{3d}$ (region 4) begins to increase on the eyelids of each billow, whereas $\mathcal{SH}_{3d}$ remains small or negative in that area (figure 12*c*). This implies that as time progresses, the increase in positive $\mathcal{SH}_{3d}$ on the eyelids results from the formation of shear-aligned convective rolls with circulations tilted against the 2-D shear (figure 13). Vortex tubes at the periphery of the billows also undergo stretching, as quantified by $\mathcal{A}_{3d}$. Stretching occurs when denser fluid descends on the upper right portion of the billow under the action of gravity, while lighter fluid ascends on the lower left (figure 12(*h*), region 6).

During this phase of maximum growth, negative $\mathcal{R}_{3d}$ emerges at the margins of the billows (figure 12*f*). Consequently, the volume-averaged value is negative (figure 12(*a*), indicated by the blue curve at $t = t_{\sigma_{3d}}$). This suggests that the background mean flow

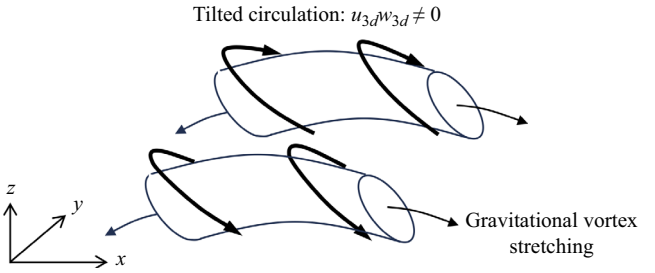

Figure 13. Schematic showing shear-aligned convective rolls tilting and stretching to form positive $\mathscr{SH}_{3d}$ and $\mathscr{A}_{3d}$, respectively.

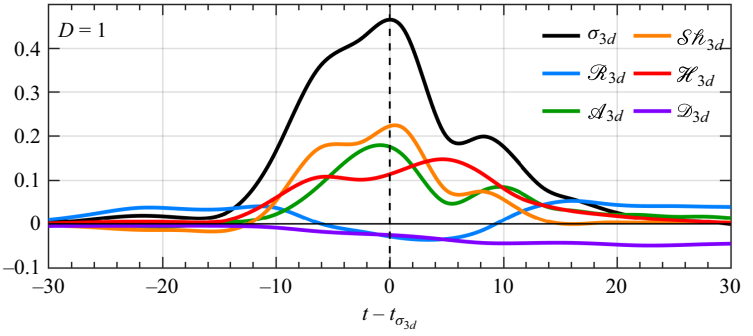

Figure 14. Dominant stationary mode when $D = 1$. As in figure 10.

contributes little to the 3-D perturbation kinetic energy in this instance. Instead, the perturbation energy is partially created by buoyancy production, but is predominantly due to shear production and the stretching of vortex tubes as discussed above.

In the case $D = 1$, although the oscillatory mode is unstable, the dynamics is governed primarily by the stationary mode. The perturbation energy terms evolve similarly to the case $D = 0.5$ (compare figures 12(*a*) and 14). This is interesting because $Ri_{min} = 0.15$, which is outside the range 0.065–0.13 where the SCI is expected based on secondary stability analysis of an isolated shear layer (Klaassen & Peltier 1991), yet the roll motions are visible, for example, on the right-hand face of figure 9(*f*). We conclude that as in the case $D = 0.5$, the SCI gives rise to shear-aligned convection rolls, consistent with positive values of $\mathscr{H}_{3d}$. The dominant source terms are again $\mathscr{SH}_{3d}$ and $\mathscr{A}_{3d}$ (figure 14).

4.4. *The SSI and pairing*

We discuss the SSI and pairing separately as they affect $\mathscr{K}_{3d}$ negligibly. The SSI grows on the braids of the primary billows where the flow is nearly parallel and the shear is intensified by the strain of the large billows (Corcos & Sherman 1976; Staquet 1995; Smyth 2003; Mashayek & Peltier 2012*a*). Staquet (1995) and Smyth (2003) find that the SSI tends to occur at higher Re_0. When $D < D_c$, the initial mean flow resembles a single shear layer with increased thickness and velocity change, i.e. with a larger Reynolds number. Therefore, the SSI may occur, depending on the initial noise field. An example is seen in figure 9(*f*). This secondary instability plays a notable role in generating turbulent mixing (to be discussed in § 5). At $t = t_{\sigma_{3d}}$, when σ_{3d} is a maximum, the enstrophy of the spanwise component $\mathscr{Z}_y$ (figure 15*b*) is significantly stronger than that of the other two components

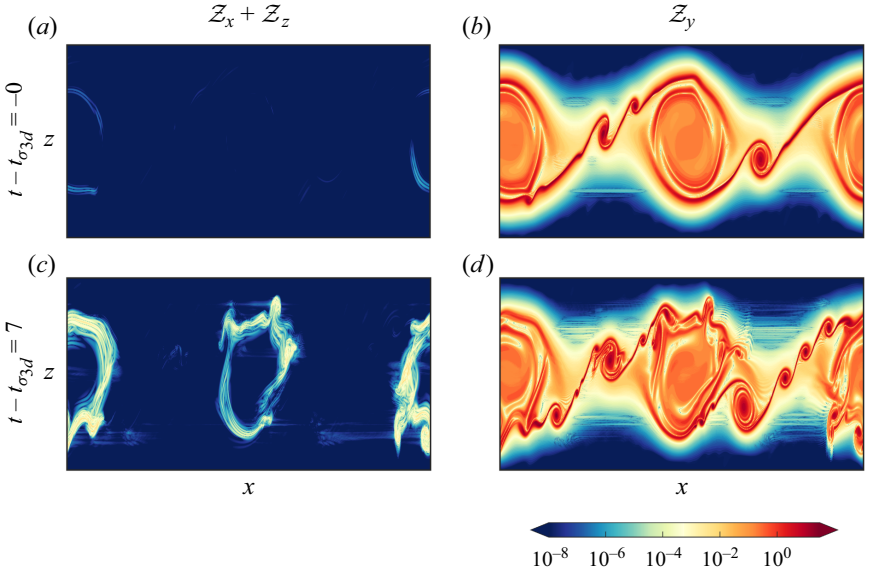

Figure 15. Spatial distribution of enstrophy during and after maximum secondary instability growth. Data are from a sample simulation in the $D = 1$ ensemble: (a,c) x and z components combined; (b,d) y component. (a,b) are both at $t - t_{\sigma_{3d}} = 0$, and (c,d) are at $t - t_{\sigma_{3d}} = 7$. Horizontal streaks are artefacts of limited spatial resolution.

combined, $\mathcal{Z}_x + \mathcal{Z}_z$ (figure 15a). The same is true for later times (figures 15(c,d) in the SSI-affected region), further confirming the 2-D nature of the SSI.

Secondary billows can be created either in pairs straddling the braid stagnation point or individually (Smyth 2003), as seen at $t - t_{\sigma_{3d}} = 7$ in figure 15(d). Between the large billow cores, a pair of smaller billows emerges at the stagnation point. The pair eventually merges and becomes a larger single vortex, which then creates its own tertiary shear instability in its surroundings, a vivid illustration of a self-similar downscale energy cascade. Other secondary billows developed away from the stagnation point are advected outwards by the extensional strain.

Vortex pairing is also affected by a nearby shear layer. Pairing is more likely to occur when D is small (e.g. $D = 0$ and 0.5), due to small Ri_{min} (figure 9b). L22 found that pairing is laminar (i.e. it occurs prior to the onset of turbulence) in cases with Ri_{min} less than 0.14, and we expected this to remain true in the present cases where Ri_{min} is considerably smaller. However, figure 9(c) indicates turbulent pairing. This is likely due to the difference in shape between the present shear layer and the single hyperbolic tangent profile assumed in L22. When $D \sim 0$, pairing precedes the onset of the SSI, leading to the disappearance of alternate braids. Subsequently, if the braids are not yet turbulent, then the SSI is likely to appear. The timing of turbulence onset, which itself depends on the choice of initial perturbation (L22), partly determines the occurrence of pairing and the SSI.

5. Turbulent mixing

A neighbouring unstable shear layer could influence turbulent mixing through its impact on the route to turbulence. We test this possibility by investigating three mixing properties: the mixing rate $\mathscr{M}$, the dissipation rate ϵ, and the mixing efficiency η, in both instantaneous (figure 16) and cumulative (figure 18) forms.

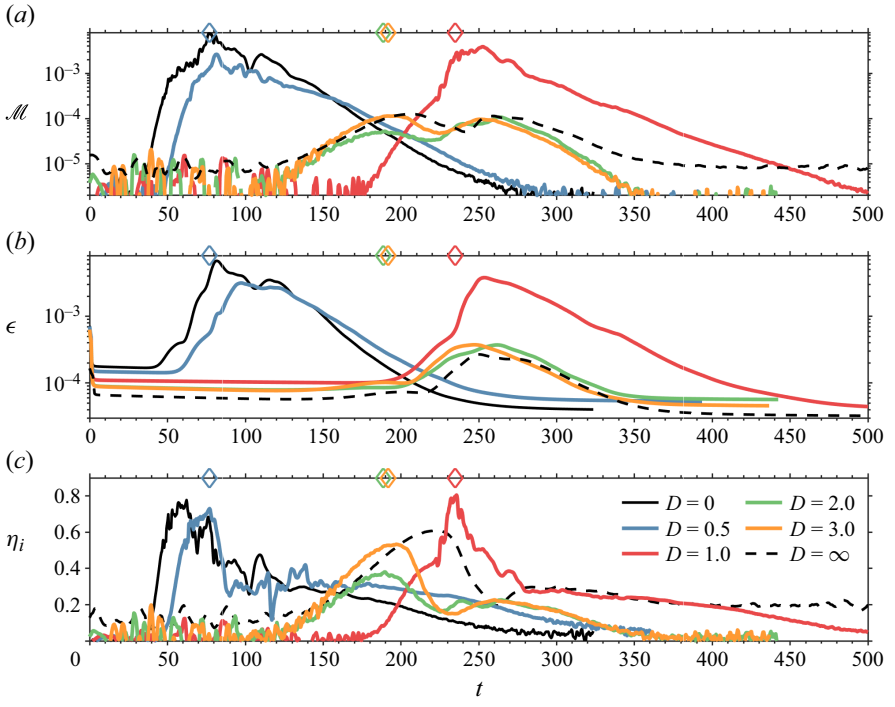

Figure 16. Time variation of the instantaneous (*a*) mixing rate, (*b*) total dissipation of the kinetic energy, and (*c*) mixing efficiency, with varying D. For clarity, only one ensemble member is included for each case of different D. Note that the magnitude and timing of the peak can be slightly different, but the overall trend is similar between the ensemble cases. The solid and dashed black curves are the case with the isolated shear layer. A running mean is carried out for all curves. Diamonds correspond to the snapshots in figure 17.

5.1. *Instantaneous mixing properties*

We first examine cases with an isolated shear layer, namely, $D = 0$ and $D \to \infty$, to set the stage for cases with $D \sim O(1)$. When $D = 0$, mixing efficiency peaks as the billows roll up ($t \sim 60$, black curve in figure 16*c*). At this pre-turbulent stage, the mixing rate is large (figure 16*a*) due to sharp scalar gradients, while the dissipation rate (figure 16*b*) remains small, and mixing efficiency is therefore large (Winters *et al.* 1995; Caulfield & Peltier 2000; Smyth & Moum 2001; Smyth 2020). Subsequently, the billow structure collapses due to the SCI (§ 4), leading to an increase in both mixing and dissipation rates. Thus mixing efficiency is reduced at $t \sim 70$ as the flow becomes turbulent. As the billows pair and merge into a single large vortex ($t \sim 110$), the mixing and dissipation rates begin to rise.

In the case $D \to \infty$, Ri_{min} doubles to 0.16. Therefore, mixing is visibly weaker than at $D = 0$ (compare black solid and dashed curves in figure 16*a*). However, since the dissipation rate is also smaller, the peak mixing efficiency at $t \sim 208$ ($\eta_i = 0.63$) for $D \to \infty$ is not very different from the peak value for $D = 0$ at $t \sim 62$ ($\eta_i = 0.78$). The two peaks of $\mathscr{M}$ are associated respectively with the breakdown of the billow and with mixing due to fully developed turbulence (cf. Kaminski & Smyth 2019, L23).

When $D = 0.5$, the mixing characteristics resemble those at $D = 0$. Mixing efficiency exhibits a peak during roll-up (as $t = 76$, marked by the blue diamond in figure 16*c*). Strong mixing, quantified by the buoyancy variance dissipation rate χ' (2.19), begins along the braids and extends inwards through overturned layers surrounding the core (figure 17*a*).

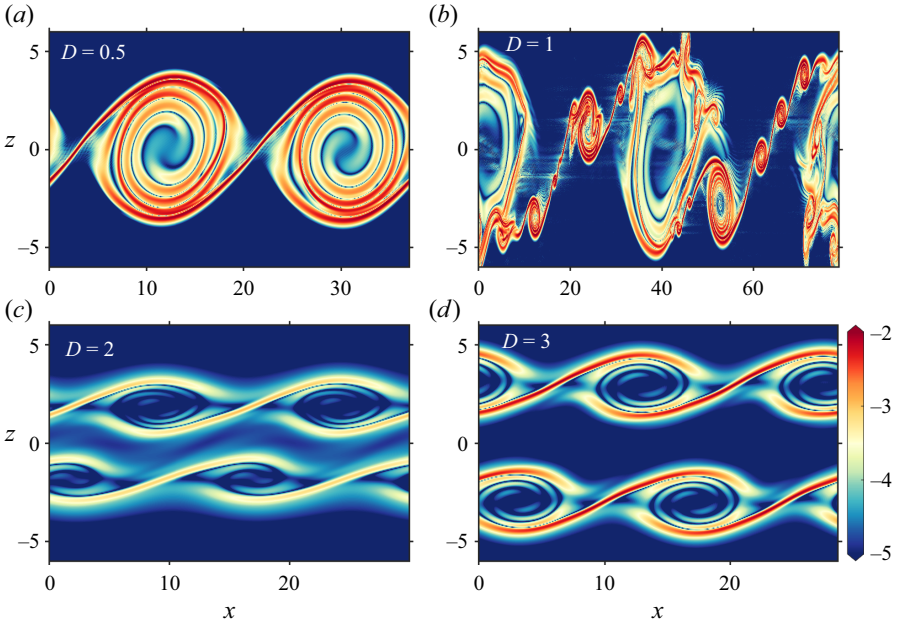

Figure 17. An x–z slice of the buoyancy variance dissipation rate $\log \chi'$ when the instantaneous mixing efficiency η_i is a maximum for (a) $D = 0.5$, (b) $D = 1$, (c) $D = 2$, and (d) $D = 3$. The snapshots for different D cases correspond to the diamond symbols in figure 16. In (b), horizontal streaks are artefacts of limited spatial resolution.

When $D = 1$, the time at which the billows roll up is the latest compared with other cases of D, consistent with its smallest growth rate (figure 4). The increase of mixing efficiency begins at $t \sim 180$ (red curve in figure 16c). Subsequently, the mixing rate increases rapidly due to the amplifying KH billow. At $t = 217$, the 2-D kinetic energy reaches its maximum, while dissipation remains relatively weak, accounting for the highly efficient mixing. Before the SCI collapses the KH billow structure, the SSI emerges along the braids. The emergence of the SSI leads to a surge of highly efficient mixing ($t = 215$–235 in figure 16a). Mixing is most intense in the braids, where it coincides with the secondary KH billows (figure 17b), and is most efficient at $t = 235$ (red diamond) because the secondary billows have not yet become turbulent, with $\eta_i \sim 0.8$ (figure 16c).

The SSI billows travel along the braids towards the primary KH billow, and then intermingle with the shear-aligned convective rolls at the eyelids (at $x = 40$, figure 17b). The primary KH billow then collapses, and the flow becomes more turbulent ($t \sim 250$). At this time, the mixing and dissipation rates approach their peak values, coinciding with a precipitous drop in the mixing efficiency (figure 16c).

The regime $D > D_c$, in which the oscillatory instability dominates (§ 3), is typified here by the cases $D = 2$ and $D = 3$. Both the mixing rate and dissipation rate are weak compared to cases where stationary mode dominates, e.g. $D = 0$, 0.5 and 1 (figures 16a,b). This weakening is due to the stronger stratification, which tends to damp both the SCI and pairing. In addition, the mutual interference of neighbouring billows suppresses the growth of the primary KH instability, leading to reduced overturning and 3-D convection, hence smaller $\mathscr{M}$ (compare $D = 2$ and $D = \infty$ in figure 18a).

While the general pattern of mixing, dissipation, and mixing efficiency remains largely consistent across all cases when $D > D_c$, there is a reduction in mixing efficiency as $D \to D_c^+$ (compare peak values for $D = \infty$, $D = 3$ and $D = 2$ in figure 16c). This reduction

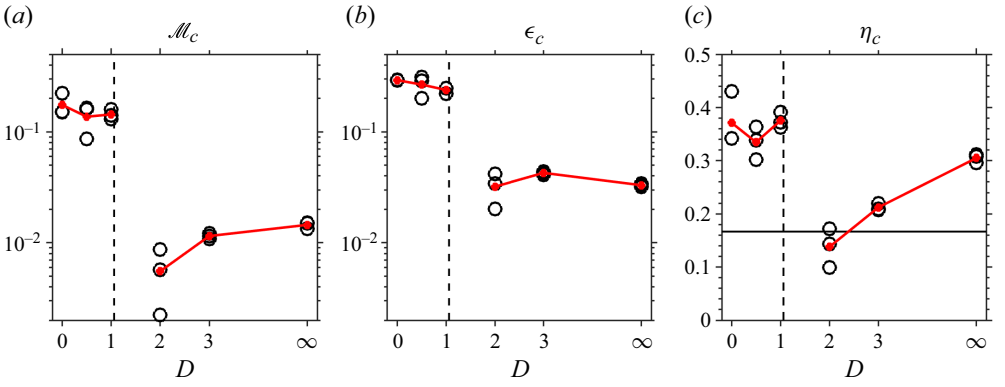

Figure 18. Dependence of (*a*) cumulative mixing, (*b*) cumulative dissipation, and (*c*) cumulative mixing efficiency on D. All ensemble cases are plotted. Red curves are the ensemble mean. The end time for the time integral is when $\mathscr{M} = \mathscr{D}_p$. The vertical dashed lines denote the critical separation distance D_c. The horizontal line denotes the canonical $\eta_c = 1/6$ suggested by Osborn (1980).

mainly reflects the diminished mixing rate $\mathscr{M}$ observed at smaller values of D. As shown in figures 17(*c*) and 17(*d*), χ' is less pronounced in case $D = 2$ compared to case $D = 3$. This suggests that as the nonlinear interaction between the upper and lower shear layers intensifies, mixing is suppressed.

5.2. *Cumulative mixing properties*

We next investigate the dependence of the cumulative mixing ($\mathscr{M}_c$), dissipation (ϵ_c) and mixing efficiency (η_c) on the separation distance D. When $D < D_c$, the net mixing and dissipation are ∼1 order of magnitude larger than when $D > D_c$ (figures 18*a*,*b*). There is less disparity in η_c, indicating an approximate balance between mixing and dissipation that tends to preserve mixing efficiency. Even so, mixing is typically more efficient by a factor ∼2 when $D < D_c$ compared to when $D > D_c$. At the extremes $D = 0$ and $D \to \infty$, η_c takes the high values (0.3–0.4) expected for an isolated shear layer (Winters *et al.* 1995; Caulfield & Peltier 2000; Smyth, Moum & Caldwell 2001).

In the oscillatory regime, the overall reduction in total amount of mixing as D approaches D_c from above may be attributed to the suppression of both the primary KH instability (due to interference between neighbouring billows impeding the phase-locking of resonant waves, as discussed in § 3) and secondary instabilities. The SCI, which plays a major role in driving mixing, can be impacted by both the reduced overturning in the suppressed primary KH instability and the neighbouring effect (§ 4.2). This suppression of the SCI becomes more pronounced as $D \to D_c^+$, potentially leading to a complete prevention of mixing – auxiliary simulations with $D = 1.5$, not shown here, failed to generated detectable instability or mixing. While $\mathscr{M}_c$ decreases as $D \to D_c^+$, there is little corresponding change in total dissipation (figure 18*b*), leading to an overall decrease in mixing efficiency.

In the stationary regime $D < D_c$, there is a slight tendency towards stronger mixing and dissipation (figures 18*a*,*b*) with decreasing D. This is likely associated with the slight reduction of Ri_{min}.

5.3. *Emergence of marginal instability*

Geophysical stratified shear flows are often in a state of marginal instability (MI), wherein the mean flow fluctuates around a stability boundary approximated by $Ri_g = 1/4$ (see

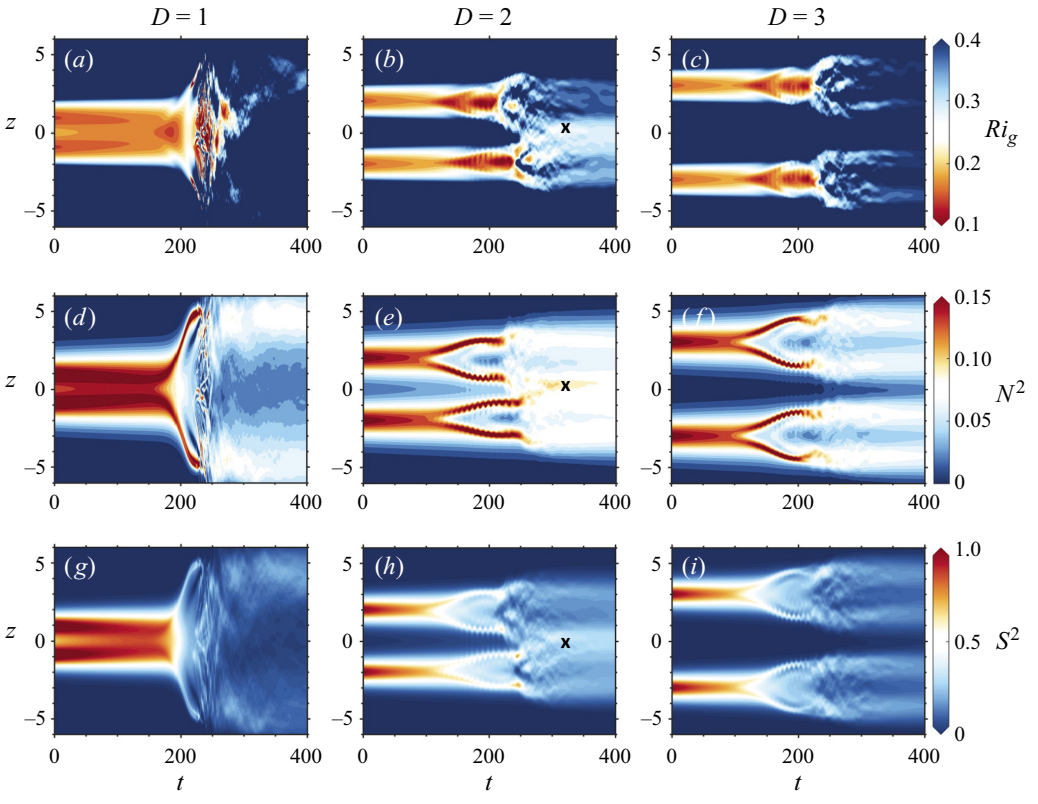

Figure 19. Horizontally averaged time series of (*a–c*) Ri_g, (*d–f*) N^2, and (*g–i*) S^2. The symbol x indicates the potential location for MI to occur.

Smyth (2020), for a recent review). In the present simulations, we find MI-like behaviour when $D = 2$ (figures 19*b*,*e*,*h*). As turbulence decays ($t \sim 250$), a layer of near-critical Ri_g (i.e. clustered around a value near 1/4) emerges around $z = 0$ (figure 19(*b*), symbol x). This near-critical Ri_g corresponds to a new stratified shear layer that forms between the two original layers (figures 19*e*,*h*) as mixing brings fluid from the upper and lower turbulent layers into close contact in the middle region, leading to local amplification of the mean buoyancy and velocity gradients.

The MI appears only in a restricted range of D, namely when the instability is in the oscillatory regime ($D > D_c$) but D is not much greater than D_c. Conversely, for $D < D_c$, the mixing characteristics resemble those of a typical KH instability, where both stratification and shear are smoothed due to strong overturning (figures 19*d*,*g*). This leads to an increase of Ri_g towards a stable state (figure 19*a*). When D is much greater than D_c, e.g. $D = 3$, the upper and lower shear layers remain too distant to overlap despite their expansion. Consequently, the weakly stratified and weakly sheared middle layer (at $z = 0$) persists (figures 19*f*,*i*) such that Ri_g is much greater than 1/4 (figure 19*c*).

6. Summary

We have investigated the instabilities of a pair of shear layers. When the layers are either unseparated or separate to an infinite extent, flow evolution is driven by the classical

KH instability. Our primary focus, however, is cases characterized by a finite, non-zero separation distance D.

In the small-amplitude limit, we find two distinct regimes: (1) a stationary mode, defined by a unique maximum growth rate, dominates when $D < D_c$ (where $D_c \approx 1$ is the critical separation distance); and (2) an oscillatory mode, consisting of two modes with equal growth rates and different phase speeds, becomes unstable when $D > \tanh^{-1}\sqrt{1/3}$, and dominates when $D > D_c$. As $D \to D_c$ from below, the stationary mode is damped because the shear maximum weakens. As $D \to D_c$ from above, damping of the oscillatory mode can be understood in terms of the resonant interaction of vorticity waves.

The presence of a neighbouring shear layer alters mixing and its efficiency by introducing an alternative route to turbulence. We have extended our analysis beyond the linear regime by conducting an ensemble of three direct numerical simulations, with different initial perturbations, for each of five values of the separation distance D. The presence of a neighbouring shear layer exerts a profound influence on the evolution and wavelength of the primary instability as well as the amplitude of the resulting KH billows. The KH instability evolves most rapidly when D is close to 0, consistent with its largest growth rate. As D increases from 0 to D_c, the evolution of the instability is prolonged (consistent with its decreasing growth rate), and the wavelength and amplitude of the KH billows increase. As D increases further from D_c to infinity, the evolution time and wavelength of the instability converge to values characteristic of an isolated shear layer.

The value of Ri_{min} is higher in the oscillatory regime ($D > D_c$) and lower in the stationary regime ($D < D_c$). Important differences in both the route to turbulence and the resulting mixing can be traced back to this distinction. In the oscillatory regime, $Ri_{min} \approx Ri_0$, the SCI is suppressed due to both the influence of stratification (Klaassen & Peltier 1991) and interference from the adjacent shear layer. The CCI is now dominant. Mixing is relatively weak and inefficient. When the separation between the upper and lower shear layers is sufficiently small, a new shear layer, exhibiting MI, forms between them.

In the stationary regime ($D < D_c$), Ri_{min} is lower and the instability resembles a weakly stratified KH instability with large amplitude. The SCI creates shear-aligned convective rolls, leading to an increase in buoyancy production (similar to previous studies, e.g. Caulfield & Peltier 2000, L23). Additionally, owing to weak stratification, billows are likely to pair. As D approaches D_c from below, buoyancy production becomes less important while shear production and gravitational stretching take over as the primary mechanisms of 3-D growth. The SSI, while not contributing directly to 3-D perturbation kinetic energy, plays a significant role in generating turbulence.

The stationary mode leads to strong and efficient mixing. At the transition to the oscillatory regime, the cumulative mixing rate, dissipation rate and mixing efficiency all decrease abruptly (figure 18*c*), showing that mixing properties can be sensitive to small changes in the initial mean flow.

7. Future directions

In this study, the initial parameters Ri_0, Re_0 and Pr remain constant, with our primary focus on the impact of separation distances. Changing these parameters will alter the transition process in various ways. For example, a different Ri_0 may alter the growth of KH instability, subharmonic instability and 3-D secondary instabilities. Turbulent mixing and the potential for marginal instability would consequently be affected in ways that are

difficult to anticipate. Moreover, varying Ri_0 while fixing Ri_{min} could isolate the effect of the separation distance D.

Increasing Re_0 is essential for simulating geophysical flows. This increase introduces a variety of secondary instabilities, which could be affected by the presence of a neighbouring shear instability. The increase of Re_0 facilitates exploration of approaching the critical separation distance ($D \sim D_c$), as the KH instability may transition to turbulence even when heavily damped by a neighbouring instability.

While $Pr = 1$ is applicable to air, higher values are more realistic for water. A higher Pr opens the possibility of a Holmboe-like instability when the mean buoyancy changes more abruptly with height than does velocity. Future studies will explore interactions of nearby Holmboe instability. This may give rise not only to KH-like instability (involving vorticity wave interaction) and Holmboe-like instability (involving vorticity and gravity wave interaction) but also to Taylor–Caulfield instability (interaction between two gravity waves; see Lee & Caulfield 2001; Smyth & Carpenter 2019), depending on the separation distance. Moreover, the scouring motion induced by Holmboe waves could be affected by the adjacent shear instability.

The variability in mixing parameters at varying separation distances has significant implications for the estimation of mixing in geophysical flows, particularly those characterized by the presence of neighbouring shear instabilities (e.g. Desaubies & Smith 1982; Moum *et al.* 2011). For the parameter values used here, the mixing efficiency ranges from ∼0.14 to ∼0.37, depending on the separation distance (figure 18*c*). Under different initial parameters or varied profile structures, such as asymmetrical velocity and buoyancy profiles (e.g. Olsthoorn, Kaminski & Robb 2023), the resulting mixing could also be substantially affected by a neighbouring instability.

The exploration of the parameter space will ultimately support a comprehensive parametrization framework for capturing the influence of neighbouring shear layers in a larger-scale model. A future goal is to explore these effects in a multi-layer context, such as the interaction of breaking internal waves at ocean ridges and seamounts.

Pre-existing turbulence exerts a substantial influence on KH instabilities (Brucker & Sarkar 2007; Kaminski & Smyth 2019). Furthermore, the onset timing of shear-driven turbulence is inherently arbitrary, making the simultaneous instability of two adjacent shear layers an atypical scenario. This highlights the potential impact of a near-field turbulent event on pre-turbulent shear instabilities. Such events may alter the development of turbulence in an adjacent shear layer.

Forced stratified flows may organize into layers consisting of neighbouring strongly stratified interfaces separated by regions of weak stratification, and a significant effort has been made to understand the circumstances under which these layers form and survive (Caulfield 2021; Petropoulos, Mashayek & Caulfield 2023). While layered structures may be robust in certain scenarios, particularly in high-Pr and double-diffusive flows (Timmermans *et al.* 2008; Taylor & Zhou 2017), in other scenarios they are prone to destruction by shear. Recent efforts have described, for example, the interaction between double-diffusive staircase structures and shear-driven turbulence (e.g. Bebieva & Speer 2019; Brown & Radko 2022). In the present problem, increasing the number of layers could provide insight into the development of turbulence in these multilayered flows.

Supplementary movies. Supplementary movies are available at https://doi.org/10.1017/jfm.2024.387.

Acknowledgements. This paper is part of the first author's PhD thesis at Oregon State University. We appreciate useful input from advisory committee members J. Moum, J. Liburdy, J. Nash and B. Pearson. We appreciate J. Carpenter's advice on the damping of the oscillatory mode (figure 8), and J. Taylor's work in creating and curating DIABLO. The paper has benefited from the comments of the editor and the

reviewers. We acknowledge high-performance computing support on Cheyenne (doi:10.5065/D6RX99HX) provided by NCAR's Computational and Information Systems Laboratory, sponsored by the US National Science Foundation.

Funding. This work was funded by the US National Science Foundation under grant OCE-1830071. A.K.K. was supported as the Ho-Shang and Mei-Li Lee Faculty Fellow in Mechanical Engineering at UC Berkeley.

Declaration of interests. The authors report no conflict of interest.

Data availability statement. DIABLO is available at https://github.com/johnryantaylor/DIABLO. Output data are available on request to the corresponding author.

Author ORCIDs.
Chih-Lun Liu https://orcid.org/0000-0001-5134-7993;
Alexis K. Kaminski https://orcid.org/0000-0002-4838-2453;
William D. Smyth https://orcid.org/0000-0001-5505-2009.

References

ALFORD, M.H. & PINKEL, R. 2000 Observations of overturning in the thermocline: the context of ocean mixing. *J. Phys. Oceanogr.* **30** (5), 805–832.

BEBIEVA, Y. & SPEER, K. 2019 The regulation of sea ice thickness by double-diffusive processes in the Ross Gyre. *J. Geophys. Res.: Oceans* **124**, 7068–7081.

BROWN, J. & RADKO, T. 2022 Disruption of Arctic staircases by shear. *Geophys. Res. Lett.* **49**, e2022GL100605.

BRUCKER, K. & SARKAR, S. 2007 Evolution of an initially turbulent stratified shear layer. *Phys. Fluids* **19**, 105105.

CARPENTER, J.R., TEDFORD, E.W., HEIFETZ, E. & LAWRENCE, G.A. 2013 Instability in stratified shear flow: review of a physical interpretation based on interacting waves. *Appl. Mech. Rev.* **64** (6), 060801.

CAULFIELD, C.P. 2021 Layering, instabilities, and mixing in turbulent stratified flows. *Annu. Rev. Fluid Mech.* **53** (1), 113–145.

CAULFIELD, C.P. & PELTIER, W.R. 2000 Anatomy of the mixing transition in homogeneous and stratified free shear layers. *J. Fluid Mech.* **413**, 1–47.

CHANG, M.-H., *et al.* 2022 Internal hydraulic transition and turbulent mixing observed in the Kuroshio over the I-Lan ridge off Northeastern Taiwan. *J. Phys. Oceanogr.* **1**, 3179–3198.

CORCOS, G.M. & SHERMAN, F.S. 1976 Vorticity concentration and the dynamics of unstable free shear layers. *J. Fluid Mech.* **73**, 241–264.

DAVIS, P.A. & PELTIER, W.R. 1979 Some characteristics of the Kelvin–Helmholtz and resonant overreflection modes of shear flow instability and of their interaction through vortex pairing. *J. Atmos. Sci.* **36** (12), 2394–2412.

DESAUBIES, Y. & SMITH, W.K. 1982 Statistics of Richardson number and instability in oceanic internal waves. *J. Phys. Oceanogr.* **12** (11), 1245–1259.

FRITTS, D.C. *et al.* 2023 Kelvin Helmholtz instability 'tube' & 'knot' dynamics, Part I: expanding observational evidence of occurrence and environmental influences. *J. Atmos. Sci.* **80** (10), 2419–2437.

FRITTS, D.C., BIZON, C., WERNE, J.A. & MEYER, C.K. 2003 Layering accompanying turbulence generation due to shear instability and gravity-wave breaking. *J. Geophys. Res.: Atmos.* **108** (D8).

GEYER, W.R., LAVERY, A., SCULLY, M.E. & TROWBRIDGE, J.H. 2010 Mixing by shear instability at high Reynolds number. *Geophys. Res. Lett.* **37**, L22607.

GREGG, M.C., D'ASARO, E.A., RILEY, J.J. & KUNZE, E. 2018 Mixing efficiency in the ocean. *Ann. Rev. Mar. Sci.* **10** (1), 443–473.

HAZEL, P. 1972 Numerical studies of the stability of inviscid parallel shear flows. *J. Fluid Mech.* **51**, 39–62.

HEIFETZ, E., BISHOP, C.H., HOSKINS, B.J. & METHVEN, J. 2004 The counter-propagating Rossby-wave perspective on baroclinic instability. I: mathematical basis. *Q. J. R. Meteorol. Soc.* **130**, 211–231.

HEIFETZ, E. & GUHA, A. 2019 Normal form of synchronization and resonance between vorticity waves in shear flow instability. *Phys. Rev.* E **100** (4), 043105.

HOLLEMAN, R.C., GEYER, W.R. & RALSTON, D.K. 2016 Stratified turbulence and mixing efficiency in a salt wedge estuary. *J. Phys. Oceanogr.* **46**, 1769–1783.

HOWARD, L.N. 1961 Note on a paper of John W. Miles. *J. Fluid Mech.* **10**, 509–512.

KAMINSKI, A.K., D'ASARO, E.A., SHCHERBINA, A.Y. & HARCOURT, R.R. 2021 High-resolution observations of the North Pacific transition layer from a Lagrangian float. *J. Phys. Oceanogr.* **51** (10), 3163–3181.

KAMINSKI, A.K. & SMYTH, W.D. 2019 Stratified shear instability in a field of pre-existing turbulence. *J. Fluid Mech.* **863**, 639–658.

KLAASSEN, G.P. & PELTIER, W.R. 1985 The onset of turbulence in finite-amplitude Kelvin–Helmholtz billows. *J. Fluid Mech.* **155**, 1–35.

KLAASSEN, G.P. & PELTIER, W.R. 1989 The role of transverse secondary instabilities in the evolution of free shear layers. *J. Fluid Mech.* **202**, 367–402.

KLAASSEN, G.P. & PELTIER, W.R. 1991 The influence of stratification on secondary instability in free shear layers. *J. Fluid Mech.* **227**, 71–106.

LASHERAS, J.C. & CHOI, H. 1988 Three-dimensional instability of a plane free shear layer: an experimental study of the formation and evolution of streamwise vortices. *J. Fluid Mech.* **189**, 53–86.

LEE, V. & CAULFIELD, C.P. 2001 Nonlinear evolution of a layered stratified shear flow. *Dyn. Atmos. Oceans* **34**, 103–124.

LEWIN, S.F. & CAULFIELD, C.P. 2021 The influence of far-field stratification on turbulent mixing. *J. Fluid Mech.* **928**, A20.

LIAN, Q., SMYTH, W.D. & LIU, Z. 2020 Numerical computation of instabilities and internal waves from *in situ* measurements via the viscous Taylor–Goldstein problem. *J. Atmos. Ocean. Technol.* **37** (5), 759–776.

LIU, C.-L., KAMINSKI, A.K. & SMYTH, W.D. 2022 The butterfly effect and the transition to turbulence in a stratified shear layer. *J. Fluid Mech.* **953**, A43.

LIU, C.-L., KAMINSKI, A.K. & SMYTH, W.D. 2023 The effects of boundary proximity on Kelvin–Helmholtz instability and turbulence. *J. Fluid Mech.* **966**, A2.

MASHAYEK, A., CAULFIELD, C.P. & PELTIER, W.R. 2013 Time-dependent, non-monotonic mixing in stratified turbulent shear flows: implications for oceanographic estimates of buoyancy flux. *J. Fluid Mech.* **736**, 570–593.

MASHAYEK, A. & PELTIER, W.R. 2012*a* The 'zoo' of secondary instabilities precursory to stratified shear flow transition. Part 1 shear aligned convection, pairing, and braid instabilities. *J. Fluid Mech.* **708**, 5–44.

MASHAYEK, A. & PELTIER, W.R. 2012*b* The 'zoo' of secondary instabilities precursory to stratified shear flow transition. Part 2 the influence of stratification. *J. Fluid Mech.* **708**, 45–70.

MASHAYEK, A. & PELTIER, W.R. 2013 Shear-induced mixing in geophysical flows: does the route to turbulence matter to its efficiency? *J. Fluid Mech.* **725**, 216–261.

MILES, J.W. 1961 On the stability of heterogeneous shear flows. *J. Fluid Mech.* **10**, 496–508.

MOUM, J.N., NASH, J.D. & SMYTH, W.D. 2011 Narrowband, high-frequency oscillations in the upper equatorial ocean: part 1: intepretation as shear instabilities. *J. Phys. Oceanogr.* **41**, 397–411.

NEWSOM, R.K. & BANTA, R.M. 2003 Shear flow instability in the stable nocturnal boundary layer as observed by Doppler lidar during CASES-99. *J. Atmos. Sci.* **60**, 16–33.

OLSTHOORN, J., KAMINSKI, A.K. & ROBB, D.M. 2023 Dynamics of asymmetric stratified shear instabilities. *Phys. Rev. Fluids* **8** (2), 024501.

OSBORN, T.R. 1980 Estimates of the local rate of vertical diffusion from dissipation measurements. *J. Phys. Oceanogr.* **10**, 83–89.

PELTIER, W.R. & CAULFIELD, C.P. 2003 Mixing efficiency in stratified shear flows. *Annu. Rev. Fluid Mech.* **35**, 136–167.

PETROPOULOS, N., MASHAYEK, A. & CAULFIELD, C.P. 2023 Turbulent disruption of density staircases in stratified shear flows. *J. Fluid Mech.* **961**, A30.

SALEHIPOUR, H. & PELTIER, W.R. 2015 Diapycnal diffusivity, turbulent Prandtl number and mixing efficiency in Boussinesq stratified turbulence. *J. Fluid Mech.* **775**, 464–500.

SMYTH, W.D. 2003 Secondary Kelvin–Helmholtz instability in a weakly stratified shear flow. *J. Fluid Mech.* **497**, 67–98.

SMYTH, W.D. 2006 Secondary circulations in Holmboe waves. *Phys. Fluids* **18**, 06414.

SMYTH, W.D. 2020 Marginal instability and the efficiency of ocean mixing. *J. Phys. Oceanogr.* **50** (8), 2141–2150.

SMYTH, W.D. & CARPENTER, J.R. 2019 *Instability in Geophysical Flows*. Cambridge University Press.

SMYTH, W.D., MAYOR, S.D. & LIAN, Q. 2023 The role of ambient turbulence in canopy wave generation by Kelvin–Helmholtz instability. *Boundary-Layer Meteorol.* **187**, 501–526.

SMYTH, W.D. & MOUM, J.N. 2000 Length scales of turbulence in stably stratified mixing layers. *Phys. Fluids* **12**, 1327–1342.

SMYTH, W.D. & MOUM, J.N. 2001 3D turbulence. In *Encyclopedia of Ocean Sciences* (ed. S. Thorpe, J. Steele & K. Turekian). Academic.

SMYTH, W.D., MOUM, J.N. & CALDWELL, D.R. 2001 The efficiency of mixing in turbulent patches: inferences from direct simulations and microstructure observations. *J. Phys. Oceanogr.* **31**, 1969–1992.

SMYTH, W.D. & PELTIER, W.R. 1989 The transition between Kelvin–Helmholtz and Holmboe instability: an investigation of the overreflection hypothesis. *J. Atmos. Sci.* **46** (24), 3698–3720.

SMYTH, W.D. & WINTERS, K.B. 2003 Turbulence and mixing in Holmboe waves. *J. Phys. Oceanogr.* **33**, 694–711.

STAQUET, C. 1995 Two-dimensional secondary instabilities in a strongly stratified shear layer. *J. Fluid Mech.* **296**, 73–126.

TAYLOR, J.R. 2008 Numerical simulations of the stratified oceanic bottom boundary layer. Thesis, University of California, San Diego, CA.

TAYLOR, J.R. & ZHOU, Q. 2017 A multi-parameter criterion of layer formation in a stratified shear flow using sorted buoyancy coordinates. *J. Fluid Mech.* **823**, R5.

TIMMERMANS, M.-L., TOOLE, J., KRISHFIELD, R. & WINSOR, P. 2008 Ice-tethered profiler observations of the double-diffusive staircase in the Canada Basin thermocline. *J. Geophys. Res.* **113**, C00A02.

TSENG, Y. & FERZIGER, J.H. 2001 Mixing and available potential energy in stratified flows. *Phys. Fluids* **13** (5), 1281–1293.

TU, J., FAN, D., LIU, Z. & SMYTH, W. 2022 Scaling the mixing efficiency of sediment-stratified turbulence. *Geophys. Res. Lett.* **49** (13), e2022GL099025.

VAN HAREN, H., GOSTIAUX, L., MOROZOV, E. & TARAKANOV, R. 2014 Extremely long Kelvin–Helmholtz billow trains in the Romanche Fracture Zone. *Geophys. Res. Lett.* **41**, 8445–8451.

WINTERS, K., LOMBARD, P.N., RILEY, J.J. & D'ASARO, E.A. 1995 Available potential energy and mixing in density-stratified fluids. *J. Fluid Mech.* **289**, 115–128.

WOODS, J.D. 1968 Wave-induced shear instability in the summer thermocline. *J. Fluid Mech.* **32**, 791–800.